Supplementary Information

Ultrafast and Deep Fluoride Elimination from Emerging Fluoride-Containing Wastewater Enabled by Hydrogen Bonding Clusters of Guanidinium Engineered Cellulose

Hanchen Wei, [a, b] Feihu Bi, [b], Shijie Zhang, [a] Xiaoling Zeng, [a] Shiting Zhang, [b] Hui Zhang, [a, b] Tian Liu, [c] Liming Yang, [*, b] Guang Yang [*, a] Xubiao Luo, [*, b]

[a] Department of Material Science and Engineering, School of Material and Chemistry, Anhui Agricultural University, Hefei, Anhui 230036, China

[b] School of Life Sciences, Key Laboratory of Jiangxi Province for Functional Biology and Pollution Control in Red Soil Regions, Jinggangshan University, Ji'an, 343009, China

[c] School of Resources and Environmental Engineering, Hefei University of Technology, Hefei, 230009, P.R. China

Table of Contents

Supplementary Text S1 Chemical Reagents and Instruments

Supplementary Text S2 Fabrication of Cell-$DG_{0.5, 1, 2}$ and Cell-NH

Supplementary Text S3 Adsorption Performance Experiment

Supplementary Text S4 Continuous Flow Column Tests

Supplementary Text S5 Density Functional Theory Calculations (DFT)

Supplementary Text S6 Independent Gradient Model based on Hirshfeld partition (IGMH)

Supplementary Text S7 Molecular Dynamics Simulation (MD)

Supplementary Text S8 Purity determination of recovered CaF_2

Supplementary Text S9 Statistical Analysis

Supplementary Scheme Schematic Illustration of the synthesis of a high-density guanidine-functionalized three-dimensional network Bio-based polymer adsorbent (Cell-$DG_{0.5, 1, 2}$) for efficient removal and resource recovery of fluoride from wastewater.

Supplementary Figure 1 Schematic of the synthesis of (a) Cell-$DG_{0. 0.5, 1, 2}$ and (b) Cell-NH.

Supplementary Figure 2 ^1H NMR spectrum of T-Cell (left) and Cell-DG_0 (right) in DMSO-*d*6.

Supplementary Figure 3 a GPC curves of T-Cell and Cell-DG_0. **b** FT-IR curves of Cell, T-Cell, Cell-DG_0 and Cell-DG_2.

Supplementary Figure 4 XRD spectra of 1,3-Diaminoguanidine monohydrochloride

a and Cell、T-Cell、Cell-DG_0、Cell-DG_2 and Cell-NH **b**.

Supplementary Figure 5 TGA **a** and DSC curves **b** of Cell、T-Cell、Cell-DG_0、Cell-DG_2 and Cell-NH.

Supplementary Figure 6 SEM diagram of Cell-DG_2.

Supplementary Figure 7 Analysis of water contact angles of different grafting degree guanidine cellulose polymer adsorption materials Cell-$DG_{0,\ 0.5,\ 1,\ 2}$.

Supplementary Figure 8 Zeta potential of different grafting degree guanidine cellulose polymer adsorption materials Cell-$DG_{0,\ 0.5,\ 1,\ 2}$ at different pH values.

Supplementary Figure 9 The full FT-IR spectra of the guanidine-based cellulose polymer material Cell-DG_2 at different temperatures.

Supplementary Figure 10 Isothermal adsorption experiments of Cell-$DG_{0,\ 0.5,\ 1,\ 2}$ and their **a** Langmuir model fit **b** Freundlich model fit and Temkin model **c**.

Supplementary Figure 11 a Kinetic adsorption data: fluoride removal performance at an initias concentration of 0.5 ppm. **b** Residual fluoride concentration. **c** pseudo-second-order model fit, and **d** Weber-Morris intraparticle diffusion model curve for fluoride ions at an initial concentration of 100 ppm.

Supplementary Figure 12 Kinetic adsorption data: **a** pseudo-first-order model fit. **b** pseudo-second-order model fit, and **c** Weber-Morris intraparticle diffusion model curve for fluoride at an initial concentration of 13 ppm.

Supplementary Figure 13 Thermodynamic adsorption data. **a, b** Removal rate and adsorption capacity of F^- by Cell-DG_2 at different temperatures. **c** Graphs of Langmuir, Freundlich, and D-R fitting curves for thermodynamic isotherms. **d** Thermodynamic

adsorption. **e** lnKd-1/T curve. **f** ln Kd-1/T curve.

Supplementary Figure 14 Selective adsorption of F^- by Cell-DG_2 material. **a** Adsorption capacity of F^- in the presence of different competing ions (Cl^-, NO_3^-, SO_4^{2-}; initial F^- concentration: 13 ppm, initial competing ion concentration:13 ppm). **b** The influence pattern of different competing ions on F^- adsorption performance. **c** Enthalpy of hydration of F^-, Cl^-, Br^-, NO_3^-, I^-.

Supplementary Figure 15 Species distribution of fluoride ions in the leaching solution under different pH conditions.

Supplementary Figure 16 a XPS spectra of Cell-DG_2 before and after adsorption of fluoride. **b** High-resolution XPS spectra of F 1s, **c** N 1s, **d** C 1s and **e** O 1s.

Supplementary Figure 17 a The removal rates of the guanidyl/amino cellulose polymer materials (Cell-DG_2, Cell-NH) under different 0.5 ppm conditions. **b** The Zeta potential of Cell-DG under different concentrations of fluoride ion solutions. **c** The comparison of Zeta potential between Cell-DG and Cell-NH in aqueous solution.

Supplementary Figure 18 Changes in the Zeta potential of Cell-DG_2 under different concentrations of NaCl;

Supplementary Figure 19 FT-IR spectra of the guanidine-based polymer adsorbent Cell-DG_2 at different adsorption concentrations: **a** full spectrum, N-H bond, C=N bond and C-O-C bond. **b** changes in wavenumber with adsorption concentration.

Supplementary Figure 20 a The full spectra of the guanidine-based cellulose polymer material Cell-DG_2 at 20, 40, 60, 80, 100, 120, 140 and 160 ℃, and the FT-IR spectra of the N-H bond and C-O-C bond **b**.

Supplementary Figure 21 Molecular model and optimized configuration of the guanidine-functionalized cellulose Cell-DG polymer chain.

Supplementary Figure 22 Snapshots of the MD simulations of Cell-DG and fluoride solutions taken at 0 ns, 1 ns, 2 ns and 50 ns, respectively. Blue, cyan, red, and white balls represent N, C, O and H atoms, respectively.

Supplementary Figure 23 The number of hydrogen bonds surrounding free fluoride ions.

Supplementary Figure 24 Schematic diagram of H_2O configuration at the interface of free F^- and Cell-DG···F^-.

Supplementary Figure 25 Cell-DG captures the number of hydrogen bonds around F^-.

Supplementary Figure 26 Optimized structure of the Cell-NH•F^- complex at the B3LYP-D3/6-31G(d)/SMD(water) level of theory.

Supplementary Figure 27 Hydrogen bond energy Cell-DG···F^-.

Supplementary Figure 28 Fixed-bed setup for continuous-flow treatment of simulated fluoride-bearing wastewaters using Cell-DG_2.

Supplementary Figure 29 a Comparative analysis of FT-IR spectra for Cell-DG_2 before and after adsorption and desorption. **b** SEM image of Cell-DG_2 after 20 desorption processes.

Supplementary Figure 30 XRD pattern of recovered CaF_2 from Cell-DG_2 packed column adsorption.

Supplementary Figure 31 a Process flow diagram for treating 1 ton of fluorine-containing wastewater. **b** The subdivided cost of polymer adsorbent preparation.

Supplementary Table 1 Water-quality characteristics of selected low-fluoride streams from photovoltaic, semiconductor and lithium-ion battery industries, with complementary model-water conditions.

Supplementary Table 2 The C, H, N elemental content and mass fraction of grafted DG of Cell-DG $_{0,\ 0.5,\ 1,\ 2}$ with different guanidine salt feed ratios.

Supplementary Table 3 Specific surface area and pore volume of Cell-DG $_{0,\ 0.5,\ 1,\ 2}$.

Supplementary Table 4 Langmuir, Freundlich and Temkin isothermal adsorption model fitting parameters for F^- adsorption by Cell-DG $_{0,\ 0.5,\ 1,\ 2}$.

Supplementary Table 5 Proposed primary and proposed secondary kinetic parameters for the adsorption of F^- by Cell-DG $_{0,\ 0.5,\ 1,\ 2}$. Fluoride ions at an initial concentration of 100 ppm and 13 ppm.

Supplementary Table 6 Fitted parameters of the Langmuir, Freundlich, and Dubinin-Radushkevich (D-R) isotherm models for fluoride (F^-) adsorption by Cell-DG_2.

Supplementary Table 7 Comparison of adsorption properties (fluoride-adsorption equilibrium time, residual fluoride concentration and removal performance) of reported fluoride adsorption materials.

Supplementary Table 8 Basic thermodynamic parameters of F^- adsorption by Cell-DG_2.

Supplementary Table 9 IGM-derived geometric, energetic, and electronic descriptors for C/N-H-F- hydrogen bonds in the guanyl polymer system.

Supplementary Table 10 Water quality characteristics report on fluorine-contain

ing process water and pretreatment wastewater in the photovoltaic, semiconductor, and lithium-ion battery industries.

Supplementary Table 11 Prices of substances required to synthesize materials.

Supplementary Text S1 Chemical Reagents and Instruments

Materials. All chemicals were used as received unless otherwise noted. Microcrystalline cellulose (99%, Cell), Lithium chloride（99.99%, LiCl）, Tosyl chloride (AR, 99%), 4-Hydroxybenzaldehyde (98%, PHB), 1,3-Diaminoguanidine monohydrochloride （DG, 98%）, Triethylamine (98%, Et_3N), Potassium carbonate (AR, K_2CO_3), Tetrabutylammonium iodide (99%, TBAI) were purchased from Aladdin. sodium hydroxide (NaOH, AR), nitric acid (HNO_3, AR), lithium nitrate ($LiNO_3$, AR), sodium nitrate ($NaNO_3$, AR), sodium chloride (AR, NaCl), sodium carbonate (AR, $NaCO_3$), anhydrous sodium sulfate (AR, Na_2SO_4), Sodium iodide (NaI, AR), Potassium bromide (KBr, AR) and Sodium bicarbonate ($NaHCO_3$, AR) were purchased from Xilong Scientific Co., Ltd. Hydrochloric acid (HCl, GR) was obtained from National Pharmaceutical Group Chemical Reagents Co., Ltd. Solvent: ethyl alcohol and methanol (MeOH, AR) were all purchased from Titan Scientific. Acetone, N, N-Dimethylformamide (99.99%, DMF), N, Dimethylacetamide (99.99%, DMAC). Hydrazine hydrate (80%). Sodium fluoride (NaF) was purchased from Shanghai Yien Chemical Technology Co., Ltd.

Instruments. The molecular structures were characterized by nuclear magnetic resonance (NMR) spectroscopy on an Agilent DD2 600 MHz spectrometer from Bruker Bio Spin International. Fourier Transform Infrared (FT-IR) spectra were recorded on a Nicolei 6670 spectrometer, scanning the wavenumber range from 4000 to 400 cm^{-1}. The molecular weights and distributions of the materials determined by gel permeation chromatography (GPC), which was equipped with a PLgel 5 μm mixed column, a guard

column, and a G1316A refractive index detector. The hydrodynamic diameter and ζ potential of the nanocomposites were assessed using a Beckman Coulter Dynamic Light Scattering (DLS) instrument. Thermal stability was evaluated by thermogravimetric analysis (TGA), wherein the polymer samples were heated from 100 to 700 °C at a rate of 10 °C/min under a nitrogen atmosphere. The glass transition temperature was determined by differential scanning calorimetry (DSC). The morphology of the polymer was observed by scanning electron microscope (SEM, Hitachi S-4800). Surface elemental composition was analyzed by X-ray photoelectron spectroscopy (XPS). Prior to XPS analysis, samples were thoroughly dried and mounted on the holder, followed by instrumental calibration of the X-ray source and analyzer. All measurements were performed under ultra-high vacuum. Crystallographic structure was investigated by X-ray diffraction (XRD) on properly dried and centered samples, with data collected over a 2θ range of 10° to 80°. Nitrogen sorption isotherms were measured at 77 K using a Micromeritics 3Flex surface analyzer, and the specific surface area was calculated using the Brunauer-Emmett-Teller (BET) method. The pH of all solutions was measured with a Shanghai Leach E-201F pH meter, and fluoride ion concentrations were quantified using a PXSJ-F ion meter.

Supplementary Text S2 Fabrication of Cell-DG$_{0.5, 1, 2}$ and Cell-NH

Preparation of T-Cell:

Cellulose (5 g) and LiCl (25 g) were dried in a vacuum oven at 100 °C for 24 h. Then, 240 mL of N, N-Dimethylacetamide (DMAc) was added to the cellulose, and the mixture was heated at 120 °C for 2 h to dissolve. After cooling to 60 °C, LiCl (25 g)

was added, and the reaction was stirred for 2 h. The mixture was stored at -24 °C for 2.5 h and then reheated to 60 °C until the cellulose was completely dissolved, affording a bright yellow viscous solution. Under a nitrogen atmosphere at room temperature, triethylamine (11.88 mL) was added with stirring in an ice-water bath, and the reaction was continued for 30 mins. Subsequently, ptoluenesulfonyl chloride (8.14 g) dissolved in DMAc (20 mL) was added dropwise slowly under a nitrogen atmosphere, and the reaction proceeded at 60 °C for 24 h. After completion, the product was precipitated in an ice-water bath, washed with deionized water (100 mL) and ethanol (500 mL), filtered, and dried in a vacuum oven at 25 °C for 24 h to obtain the solid product T-Cell.

Preparation of Cell-DG_0:

T-Cell (1 g) was dissolved in DMF (30 mL). To this solution, p-hydroxybenzaldehyde (1.06 g), tetrabutylammonium iodide (TBAI, 213 mg), and potassium carbonate (K_2CO_3, 400 mg) were added. The reaction was stirred at 80 °C for 24 h. Upon completion, the solvent DMF was evaporated at 60 °C. Methanol (50 mL) was added at room temperature, and the mixture was stirred for 1-2 h. The solid product was collected by suction filtration using a Büchner funnel, washed with deionized water (50 mL) and methanol (100 mL), and dried in a vacuum oven at 50-60 °C for 24 h to obtain the solid product Cell-DG_0.

Preparation of Cell-$DG_{0.5, 1, 2}$:

Cell-DG_0 (200 mg) was dissolved in DMF (3 mL). To this solution, 1,3-diaminoguanidine hydrochloride (13, 35, 70 mg) were added, and the reaction was stirred under reflux at 130 °C for 24 h. After completion, the DMF was evaporated. The

product was soaked in methanol for 2 h and filtered. The resulting solid was washed with water and methanol.

Preparation of Cell-NH:

Cell-NH was prepared following the same procedure as described for Cell-DG, except that 1,3-diaminoguanidine hydrochloride was replaced with hydrazine hydrate to introduce amino-functionalized units.

Supplementary Text S3 Adsorption Performance Experiment.

Isothermal adsorption experiment

Isothermal adsorption experiments for materials were conducted at 25°C. Precisely weighed portions of the adsorbent (10 mg) were added to a series of centrifuge tubes containing 10 mL of fluoride solutions with initial concentrations ranging from 5 to 400 mg L^{-1} (5, 10, 20, 30, 50, 70, 100, 150, 200, 400 mg L^{-1}). The tubes were then shaken in a thermostatic shaker at 25°C and 180 rpm for 24 h. Post-adsorption: 5 mL of the suspension was withdrawn using a syringe and filtered through a 0.22 μm membrane filter. The filtrate was diluted appropriately, and the equilibrium fluoride ion concentration was determined using a fluoride ion-selective electrode. The adsorption capacity was calculated accordingly:

$$Q_e = \frac{(C_0 - C_e)V}{m} \quad (1)$$

where Q_e (mg g^{-1}) is the adsorption capacity of fluoride ions per gram of adsorbent at equilibrium. C_0 (mg/L) and C_e (mg/L) are the initial concentration and the equilibrium concentration of F^- in the aqueous solution, respectively. V (L) is the total volume of the aqueous solution, and m (mg) is the mass of the adsorbent.

The fitting was performed using Langmuir, Freundlich, and Temkin isotherm models.

The equation for the Langmuir model is as follows:

$$Q_e = \frac{Q_m K_L C_e}{1 + K_L C_e} \quad (2)$$

where C_e (mg L^{-1}) is the equilibrium concentration of F^-, Q_e (mg g^{-1}) and Q_m (mg g^{-1}) are the adsorption capacity at equilibrium and the theoretical maximum adsorption capacity, respectively, and K_L (L mg^{-1}) is the adsorption constant of the Langmuir model.

The equation for the Freundlich model is as follows:

$$Q_e = KFC_e^{1/n} \quad (3)$$

where C_e (mg L^{-1}) is the equilibrium concentration of F^-, Q_e (mg g^{-1}) is the adsorption capacity at equilibrium, and K_L is the adsorption constant of the Freundlich model.

The equation for the Temkin model is as follows:

$$Q_e = B_T \ln K_T + B_T \ln C_e \quad (4)$$

where C_e (mg L^{-1}) is the equilibrium concentration of F^-, Q_e (mg g^{-1}) is the adsorption capacity at equilibrium, B_T (kJ mol^{-1}) is the adsorption constant of the Temkin model related to adsorption heat, and K_T (L mg^{-1}) is the equilibrium binding constant.

Adsorption kinetics experiment

F^- adsorption kinetics were investigated at 25°C using adsorbents Cell-DG. A 30 mg of the material was weighed and added to a conical flask containing 30 mL of a

fluoride solution (with initial mass concentrations of 0.5 and 50 mg/L). The experiments were conducted under conditions of 25°C and 180 rpm. The residual fluoride concentration at different time intervals (0, 1, 3, 5, 10, 30, 60, 90, 150, 180, 200, 250, 300 min) was measured. Specifically, 1 mL of the suspension was sampled, filtered through a 0.22 μm microporous membrane, diluted 30-fold with deionized water, and the fluoride ion concentration was measured using a PXSJ-216F ion meter. The removal rate and adsorption capacity were calculated as follows:

$$Q_t = (C_0 - C_t)V/m \quad (5)$$

where Q_t (mg g^{-1}) is the adsorption capacity of fluoride ions per gram of adsorbent at time t (min). C_0 (mg L^{-1}) and C_t (mg L^{-1}) are the initial concentration and the concentration at time t (min) of F^- in the aqueous solution, respectively. V (mL) is the total volume of the aqueous solution, and m (mg) is the mass of the adsorbent.

The adsorption process for fluoride was investigated using pseudo-first-order and pseudo-second-order kinetic models. The fitting equations are as follows:

$$\ln\left(Q_e - Q_t\right) = \ln Q_e - k_1 t \quad (6)$$

$$\frac{t}{Q_t} = \frac{1}{k_2 Q_e^2} + \frac{1}{Q_e} \quad (7)$$

Where Q_e and Q_t (mg g^{-1}) represent the adsorption capacity at equilibrium and at time t (min), respectively; k_1 (L min^{-1}) and k_2 (g mg^{-1} min^{-1}) are the rate constants of the pseudo-first-order and pseudo-second-order models, respectively.

Competitive ion effect experiment

For the competitive ion experiments, 10 mg of the material was weighed and added to a series of conical flasks, each containing 10 mL of a fluoride solution with initial

mass concentrations of 0.5 and 50 mg/L, respectively. The competing ions investigated included Cl^-, NO_3^-, SO_4^{2-}, Br^-, I^-, PO_4^{3-}, HCO_3^-, and CO_3^{2-}, each at a concentration of 2.5 mmol/L. After adsorption equilibrium was reached, the residual fluoride concentration was measured to calculate the adsorption capacity and removal efficiency.

pH influence experiment

For the pH effect experiments, 10 mg of the material was weighed and added into a series of conical flasks, each containing 10 mL of fluoride solution with initial mass concentrations of 0.5 and 50 mg/L, respectively. The initial pH of the solutions was adjusted to a range of 2-10 using 0.1 mol/L NaOH and 0.1 mol/L HNO_3 solutions. After adsorption equilibrium was reached, the residual fluoride concentration was measured to calculate the adsorption capacity and removal efficiency.

Fluoride Removal Efficiency

For the removal efficiency tests, different masses of the adsorbent (10, 20, 50, and 100 mg) were respectively weighed and added into a series of conical flasks, each containing 10 mL of a fluoride solution with an initial concentration of 50 mg/L. The flasks were placed in a thermostatic shaker set at 25 °C and 180 rpm for 24 h to carry out the static adsorption experiments. After reaching adsorption equilibrium, 5 mL of the suspension was extracted using a syringe, filtered through a 0.22 μm membrane, and diluted appropriately. The fluoride ion concentration in the solution was then measured with a fluoride ion selective electrode, and the fluoride removal efficiency was calculated.

Thermodynamic Adsorption Experiments

A series of 10 mg adsorbent samples were weighed and added into separate vials, each containing 10 mL of a 50 mg/L fluoride ion solution. The adsorption experiments

were conducted at 298 K (25 °C), 308 K (35 °C), and 318 K (45 °C), respectively, to investigate the temperature dependence. The thermodynamic parameters, namely the Gibbs free energy change (ΔG), enthalpy change (ΔH), and entropy change (ΔS), were calculated using the following equations:

$$\Delta G = -RTlnK_d \quad (8)$$

$$K_d = 55.51 * K_L * 1000 \quad (9)$$

$$lnK_d = \frac{\Delta G}{R} - \frac{\Delta H}{RT} \quad (10)$$

where K_d is the thermodynamic equilibrium constant, K_L is the adsorption constant from the Langmuir model, R (8.314 J mol^{-1} K^{-1}) is the universal gas constant, and T (K) is the absolute temperature in Kelvin.

Supplementary Text S4 Continuous Flow Column Tests

To investigate the potential for large-scale application of the adsorbent, a fixed-bed adsorption setup was constructed. A quantity of the material (Cell-DG material) was weighed and packed into a polymethyl methacrylate column with a height of 10 cm and an inner diameter of 1.5 cm. The measured mass of the material was 10.12 g. A peristaltic pump was used to maintain a constant effluent flow rate at 6 BV/h. Then, a pre-prepared fluoride ion solution with a concentration of 200 mg/L was introduced, and the system was operated at this flow rate for 5 hours. Simultaneously, effluent samples were collected at predetermined time intervals (1, 3, 5, 10, 15, 20, 25, 30, 40, 50, 60, 80, 100, 120, 150, 180, 200, 250, 300 mins). The collected water samples were filtered through a 0.22 μm organic filter membrane, and the fluoride concentration was determined using a PXFJ fluoride ion meter.

For desorption, a peristaltic pump was employed to pass 450 mL of 0.3 mmol/L sodium hydroxide solution through the column at a flow rate of 3 BV/h. Desorption effluent was collected every 10 mins, filtered, and then analyzed for fluoride concentration in a similar manner. Three simulated fluoride-bearing wastewaters (I-III) were used to evaluate adsorption in different mixed-ion feeds. These correspond to the lithium battery recycling, lithium mica smelting slag leachate, and photovoltaic wastewater formulations, respectively. For these tests, 450 mL of each simulated wastewater was pumped through the adsorption column at 6 BV/h using a peristaltic pump.

Supplementary Text S5 Density Functional Theory Calculations (DFT)

Density functional theory (DFT) calculations were performed using the materials studio package. DFT were used to elucidate the adsorption mechanism of adsorbent materials such as Cell-DG on target ionization. Geometry optimizations and vibrational frequency calculations were carried out with the B3LYP-D3,[1-3] with the 6-31G(d,p)[4] basis set applied to all atoms. The quantum chemical calculations were done through the DMOl^3 module in Materials Studio software, using the generalized gradient approximation (GGA) as a functional option for geometry optimization and spin-unrestricted DFT optimization of the molecular model using the Perdew-Berke-Ernzerhof (PBE) correlation energy functional to further compute the binding energy.[1] The binding energy (ΔE) of Cell-DG with each ion was calculated by Eq:

$$\Delta E = E_{total} - E_{adsorbate} - E_{adsorbent} \quad (11)$$

In the equation, E_{total} (eV), $E_{adsorbate}$ (eV) and $E_{adsorbent}$ (eV) are denoted as the total

energy of the adsorption system, the energy of the adsorbed target metal ion and the energy of the adsorbed material, respectively.

Supplementary Text S6 Independent Gradient Model based on Hirshfeld partition (IGMH)

Quantum chemical calculations were performed using the ORCA 6.0 program package.[5] Geometry optimizations and vibrational frequency analyses were carried out using the B97-3c composite method.[6] This method intrinsically employs a specifically modified triple-zeta basis set (def2-mTZVP) and incorporates Grimme's D3(BJ) empirical dispersion correction along with a short-range basis set correction, providing an efficient and accurate description of geometries and non-covalent interactions. Solvation effects during the optimization phase were modeled using the Conductor-like Polarizable Continuum Model (CPCM) with water as the solvent.[7] Harmonic vibrational frequencies were computed at the same level of theory to confirm that the optimized structures correspond to true energy minima, characterized by the absence of imaginary frequencies.

To obtain highly accurate electronic energies, single-point energy calculations were subsequently performed on the optimized geometries. These high-level calculations utilized the hybrid PBE0 functional[8] in conjunction with Grimme's charge-dependent D4 dispersion correction.[9] The large def2-TZVPPD basis set,[10, 11] which incorporates diffuse functions to provide a more flexible and accurate description of the electron density, was employed. Solvation effects in the single-point calculations were identically modeled using the CPCM model in water.

To visually and quantitatively investigate the non-covalent interactions within the systems, the Independent Gradient Model based on Hirshfeld partition (IGMH) analysis[12] was performed. The IGMH analysis was conducted using the Multiwfn program (version 3.8)[13] based on the wavefunction files generated from the corresponding high-level single-point calculations.

Supplementary Text S7 Molecular Dynamics Simulation (MD)

Cell-DG，H_3O^+，F^- molecules are described by using the OPLS-AA force field. The LJ interaction between atoms is calculated by the Lorentz-Berthelot combination rule. The short-range non-bonding interaction is truncated at 1.20 nm, and the long-range electrostatic interaction is calculated using the PME summation method. The H_2O molecule adopts the TIP4P-2005 model, which has virtual sites and uses the SETTLE algorithm to rigidly constrain the water molecule. The calculation time step is 2 fs, and the xyz directions are periodic boundary conditions. The initial configuration adopts the fastest descent algorithm for energy minimization. NPT simulations lasting 50 ns were conducted under 298.15 K and 1 bar. The Nosé-Hoover coupling methods was employed to control the temperature, with time constants of 2 ps. The pressure was regulated using Parrinello-Rahman methods. The pressure control mode is isotropic. All MD simulations were conducted using Gromacs v5.0.7.

Supplementary Text S8 Purity determination of recovered CaF_2

The recovered CaF_2 product was obtained from the fluoride-rich desorption solution by $CaCl_2$ precipitation, followed by filtration, washing with deionized water, and drying at 60 °C. The crystalline phase was first confirmed by XRD (Figure S26,

PDF#35-0816). For chemical purity analysis, about 0.1000 g of dried CaF_2 was accurately weighed into a 100 mL beaker, wetted with a few drops of ultrapure water, and dissolved in 10 mL of HCl (1:1) containing 2.0 g H_3BO_3. The mixture was heated gently to near boiling until the solution became clear. After cooling, the solution was transferred to a 100 mL volumetric flask and made up to volume with ultrapure water. A blank was prepared in parallel. The solution was filtered through a 0.22 μm membrane and appropriately diluted before analysis.

Calcium was determined by ICP-OES using the Ca 317.933 nm emission line (RF power: 1150 W, plasma gas: 12 L min^{-1}, auxiliary gas: 0.5 L min^{-1}, nebulizer gas: 0.7 L min^{-1}). Calibration standards containing 0, 0.1, 0.5, 1, 2, 5, 10, and 20 mg L^{-1} Ca were prepared in the same HCl-H_3BO_3 matrix.

The CaF_2 purity was calculated as:

$$W(CaF_2) = [(C - C_0) * V * D * M(CaF_2)]/[M(\mathrm{Ca}) * E_m * 1000] * 100 \quad (12)$$

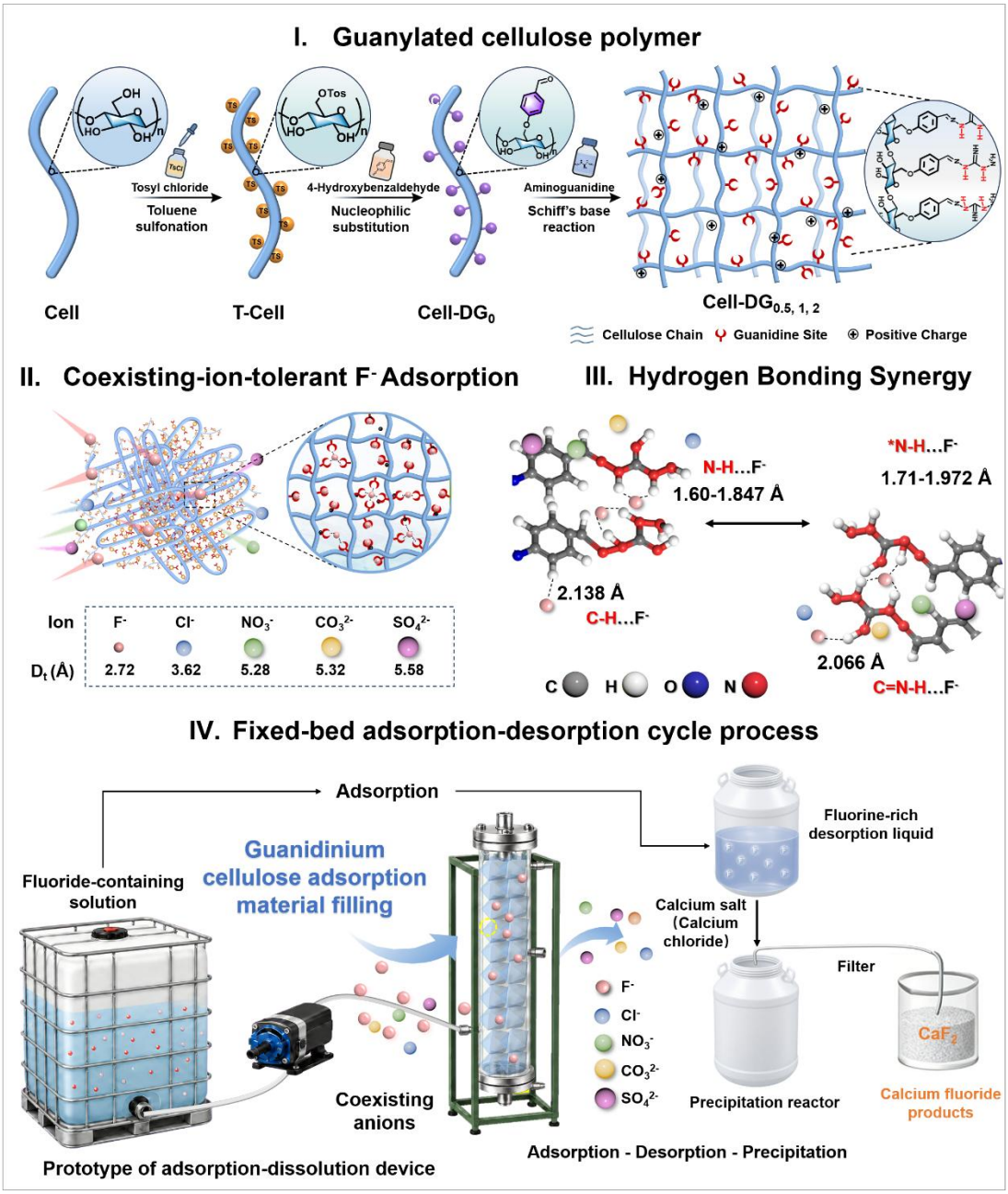
where C and C_0 are the Ca concentrations in the sample and blank, respectively (mg L^{-1}). V is the volumetric volume (L). D is the dilution factor; m is the sample mass (g). $M(CaF_2)$ = 78.074 g mol^{-1}, and $M(Ca)$ = 40.078 g mol^{-1}. Each sample was analyzed in triplicate, with RSD < 3% and spike recoveries of 95-105%.

Supplementary Text S9 Statistical Analysis

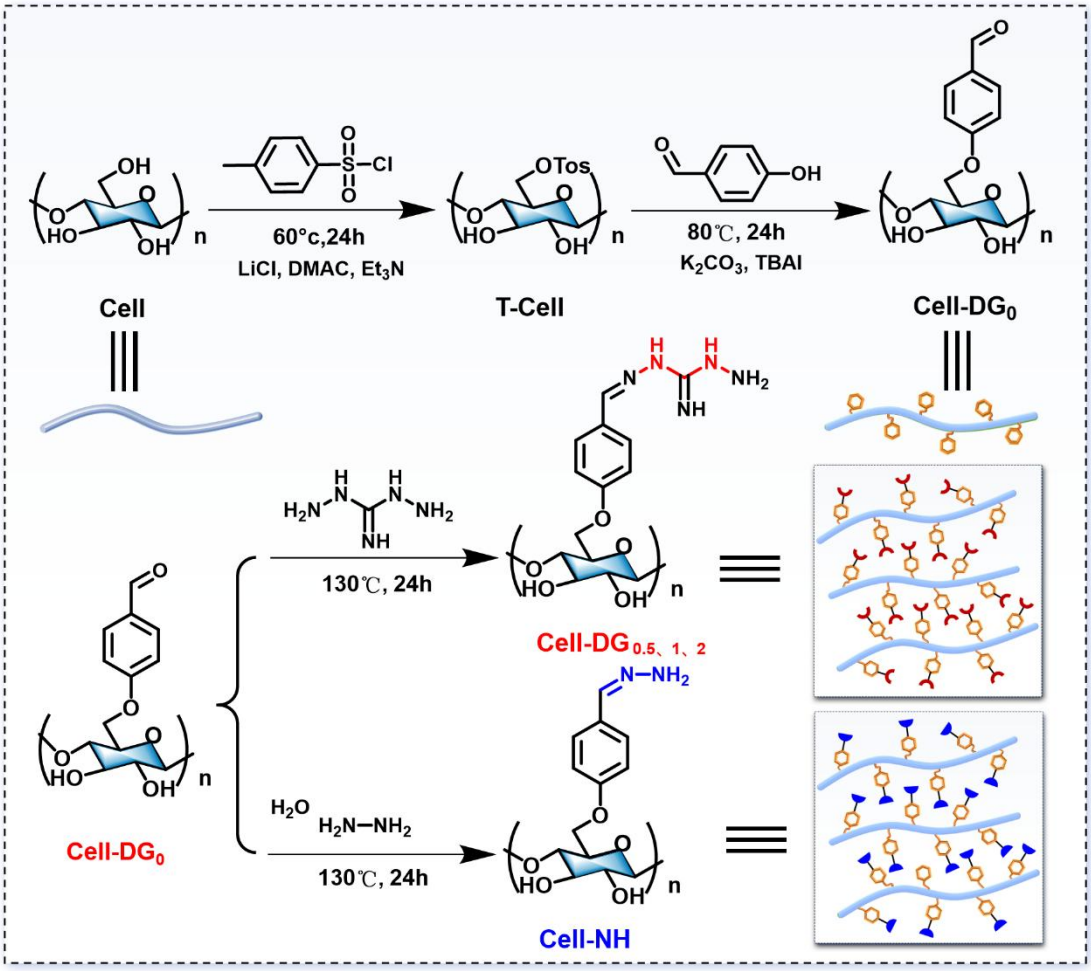
All water flow dynamics in cellular-structured scaffolds and adsorption data were collected from at least three independent replicates ($n \geqslant 3$) unless otherwise stated. Data were presented as mean ± standard deviation (SD). No data transformation or normalization was applied. Outliers were not excluded unless clearly justified by

instrumental error.

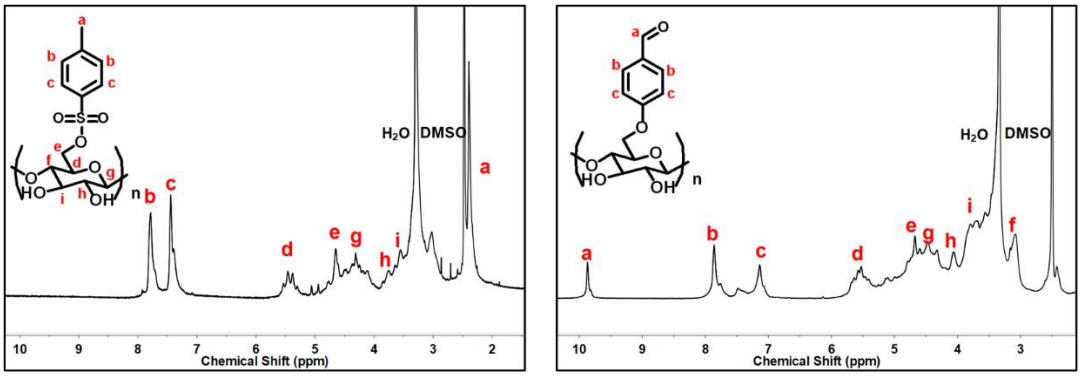
Supplementary Figures:



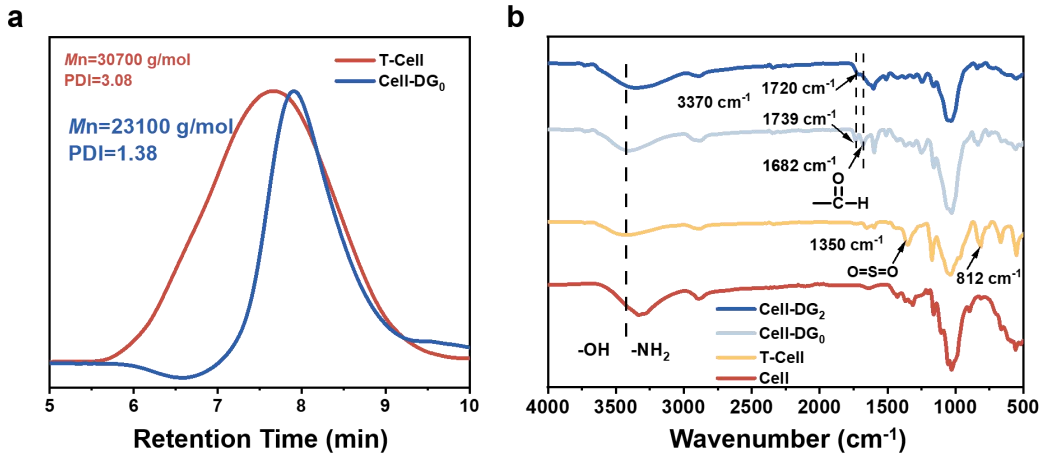
Supplementary Scheme Schematic Illustration of the synthesis of a high-density guanidine-functionalized three-dimensional network Bio-based polymer adsorbent ($Cell\text{-}DG_{0.5,1,2}$) for efficient removal and resource recovery of fluoride from wastewater.



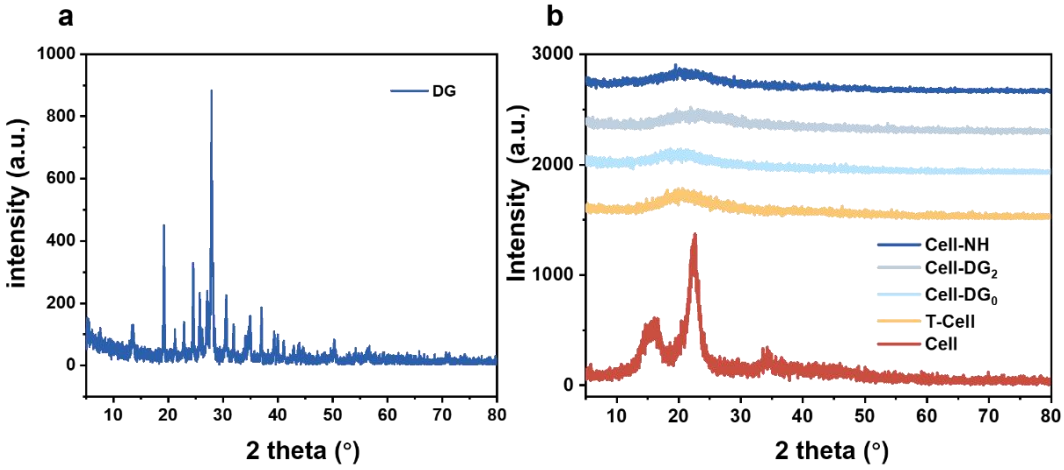
Supplementary Figure 1 Schematic of the synthesis of (a) Cell-DG$_{0,\ 0.5,\ 1,\ 2}$ and (b) Cell-NH.



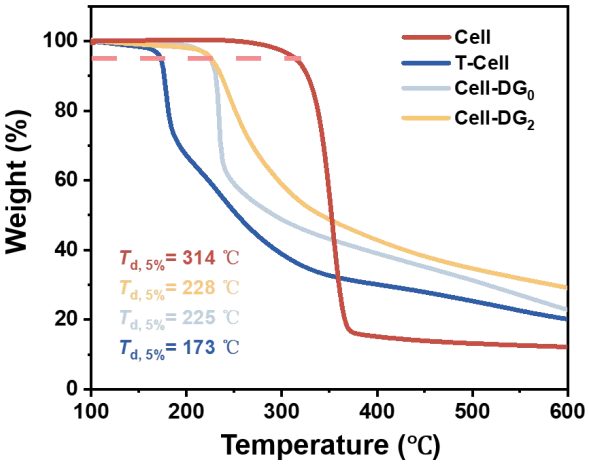
Supplementary Figure 2 ^{1}H NMR spectrum of T-Cell (left) and Cell-DG$_0$ (right) in DMSO-*d*6.



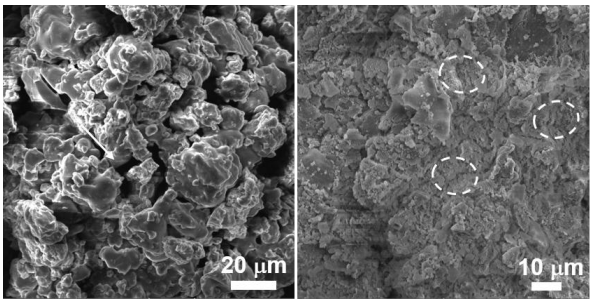
Supplementary Figure 3 a GPC curves of T-Cell and Cell-DG_0. **b** FT-IR curves of Cell, T-Cell, Cell-DG_0 and Cell-DG_2.



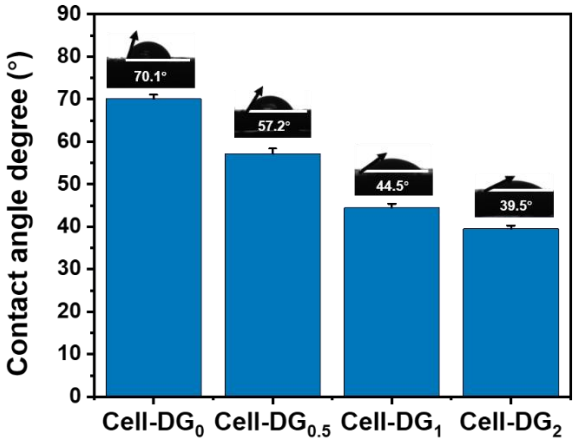
Supplementary Figure 4 XRD spectra of 1,3-Diaminoguanidine monohydrochloride a and Cell、T-Cell、Cell-DG_0、Cell-DG_2 and Cell-NH **b**.



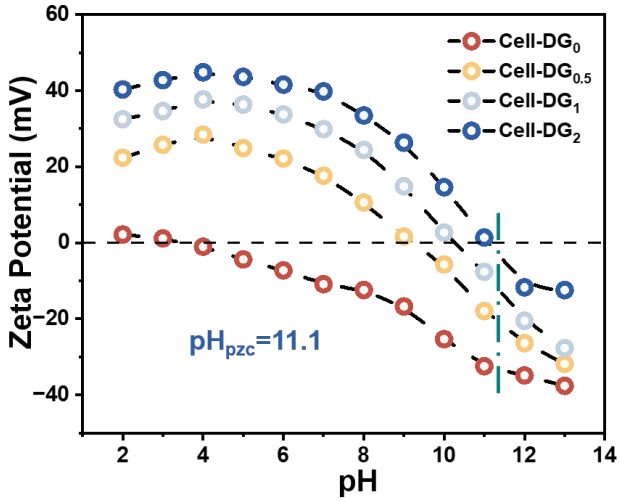
Supplementary Figure 5 TGA **a** and DSC curves **b** of Cell、T-Cell、Cell-DG_0、Cell-DG_2 and Cell-NH.



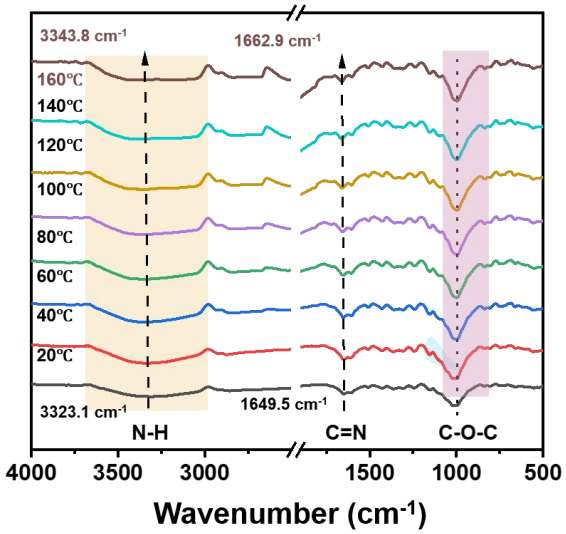
Supplementary Figure 6 SEM diagram of Cell-DG_2.



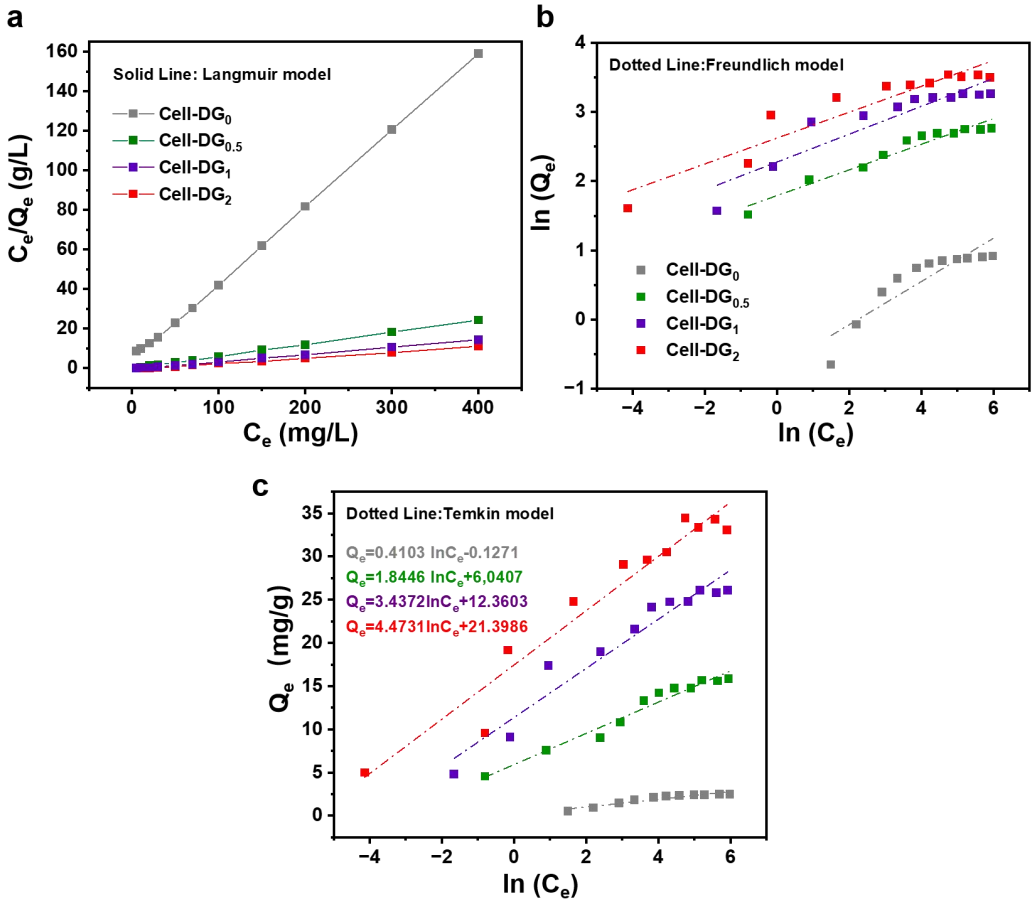
Supplementary Figure 7 Analysis of water contact angles of different grafting degree guanidine cellulose polymer adsorption materials Cell-$DG_{0,\ 0.5,\ 1,\ 2}$.



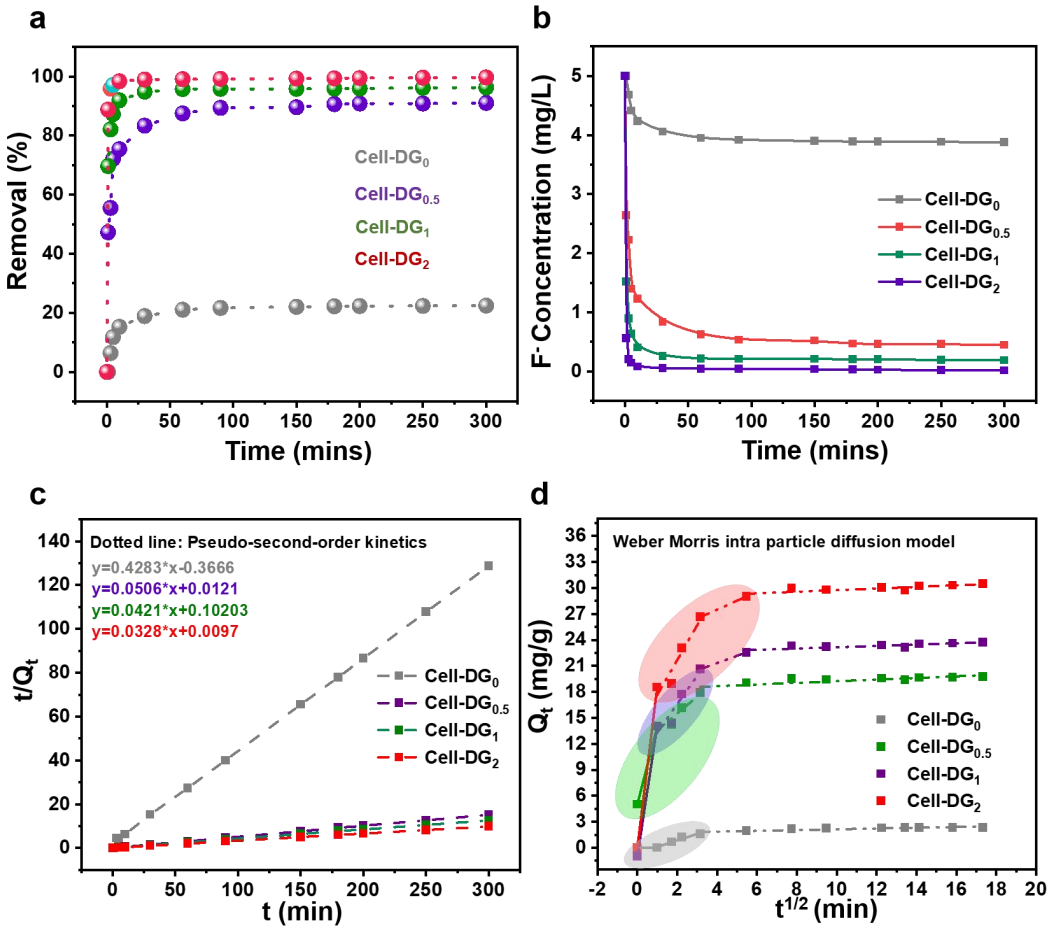
Supplementary Figure 8 Zeta potential of different grafting degree guanidine cellulose polymer adsorption materials Cell-$DG_{0, 0.5, 1, 2}$ at different pH values.



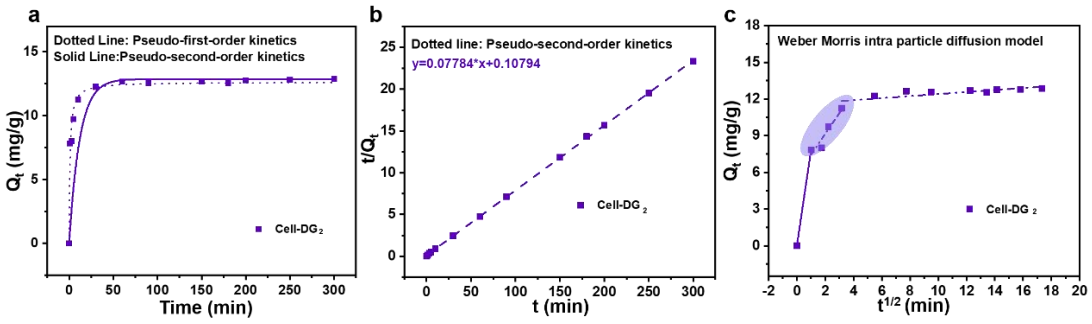
Supplementary Figure 9 The full FT-IR spectra of the guanidine-based cellulose polymer material Cell-DG_2 at different temperatures.



Supplementary Figure 10 Isothermal adsorption experiments of Cell-$DG_{0,\ 0.5,\ 1,\ 2}$ and their **a** Langmuir model fit **b** Freundlich model fit and Temkin model **c**.

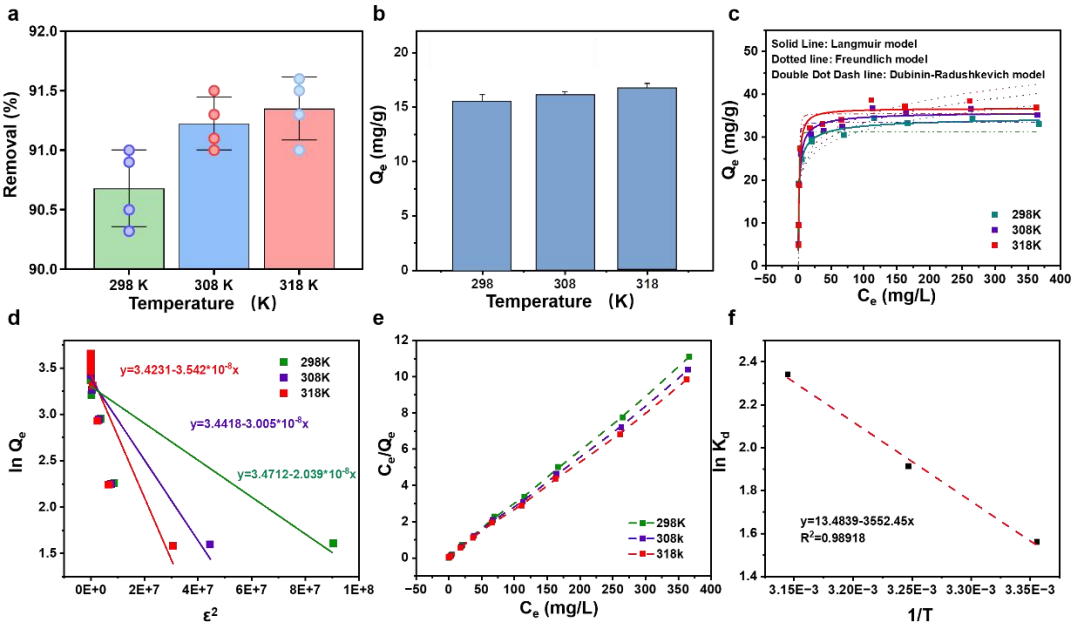


Supplementary Figure 11 a Kinetic adsorption data: fluoride removal performance at an initias concentration of 0.5 ppm. **b** Residual fluoride concentration. **c** pseudo-second-order model fit, and **d** Weber-Morris intraparticle diffusion model curve for fluoride ions at an initial concentration of 100 ppm.

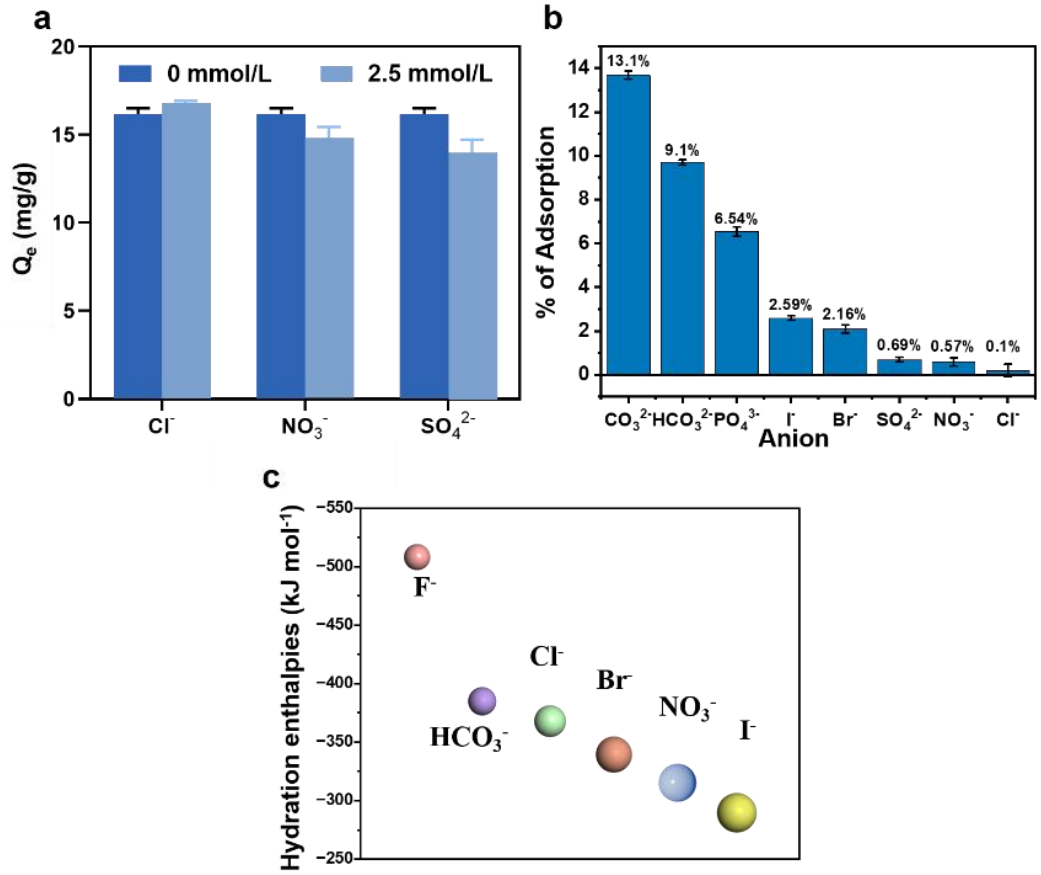


Supplementary Figure 12 Kinetic adsorption data: **a** pseudo-first-order model fit. **b** pseudo-second-order model fit, and **c** Weber-Morris intraparticle diffusion model curve

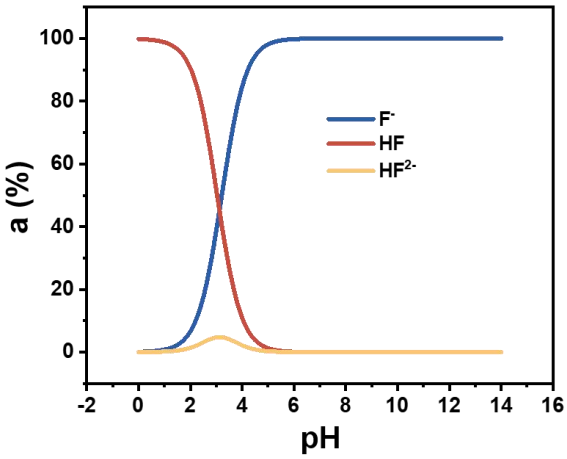
for fluoride at an initial concentration of 13 ppm.



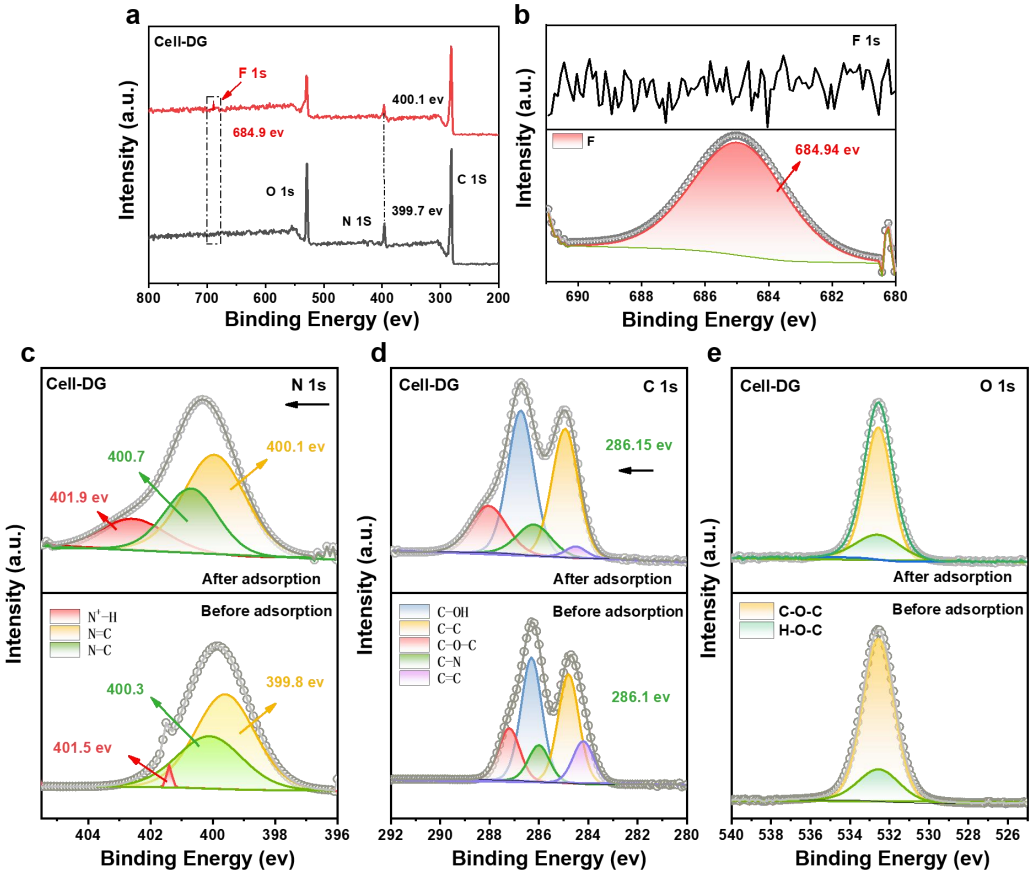
Supplementary Figure 13 Thermodynamic adsorption data. **a, b** Removal rate and adsorption capacity of F^- by Cell-DG_2 at different temperatures. **c** Graphs of Langmuir, Freundlich, and D-R fitting curves for thermodynamic isotherms. **d** Thermodynamic adsorption. **e** lnKd-1/T curve. **f** ln Kd-1/T curve.



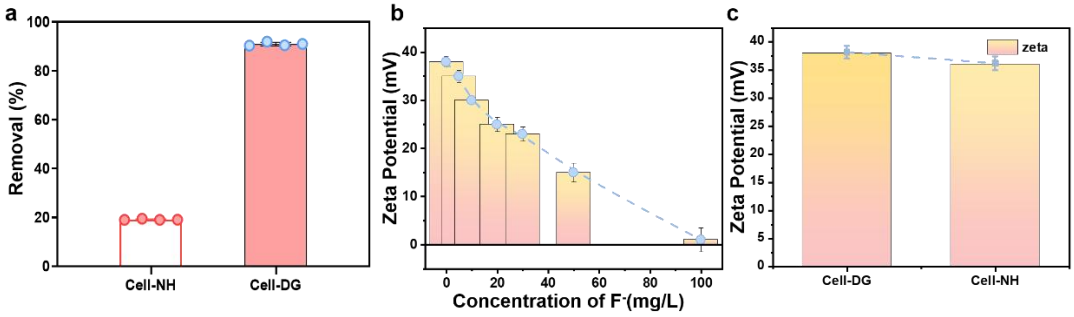
Supplementary Figure 14 Selective adsorption of F^- by Cell-DG_2 material. **a** Adsorption capacity of F^- in the presence of different competing ions (Cl^-, NO_3^-, SO_4^{2-}; initial F^- concentration: 13 ppm, initial competing ion concentration:13 ppm). **b** The influence pattern of different competing ions on F^- adsorption performance. **c** Enthalpy of hydration of F^-, Cl^-, Br^-, NO_3^-, I^-.



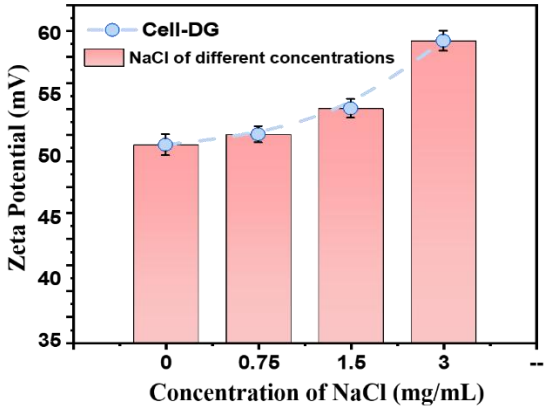
Supplementary Figure 15 Species distribution of fluoride ions in the leaching solution under different pH conditions.



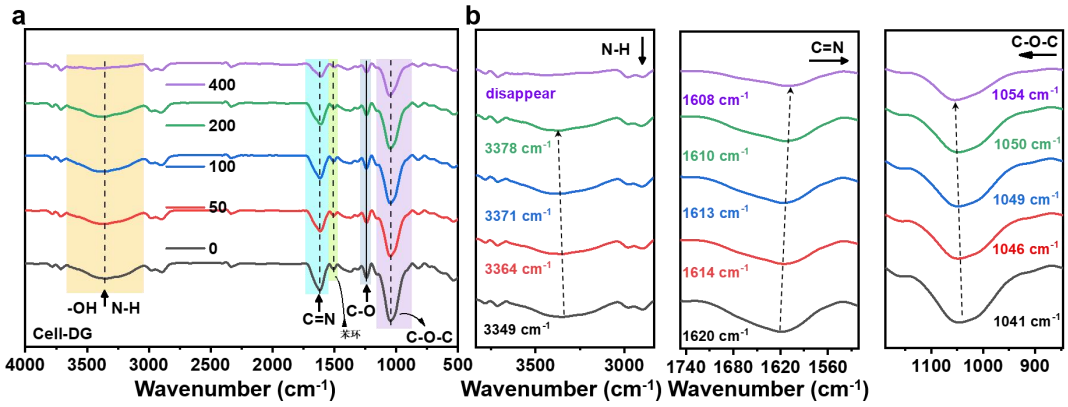
Supplementary Figure 16 a XPS spectra of Cell-DG$_2$ before and after adsorption of fluoride. **b** High-resolution XPS spectra of F 1s, **c** N 1s, **d** C 1s and **e** O 1s.



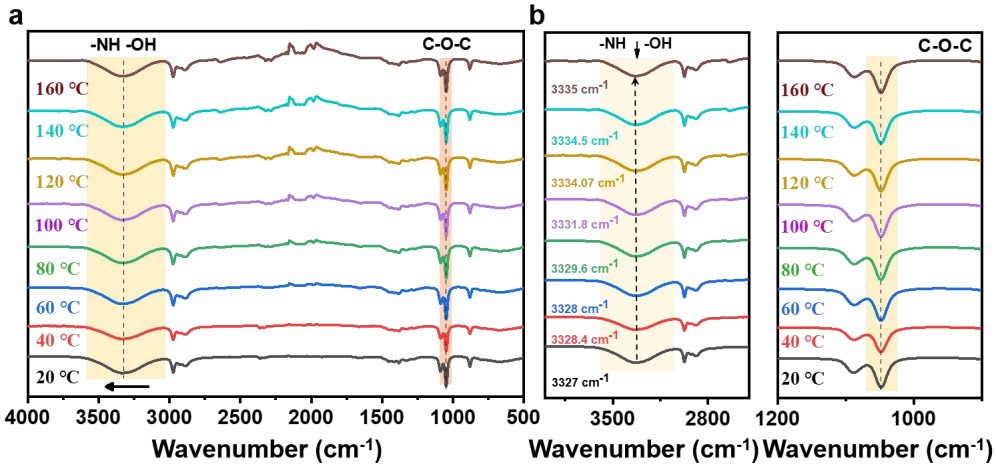
Supplementary Figure 17 a The removal rates of the guanidyl/amino cellulose polymer materials (Cell-DG$_2$, Cell-NH) under different 0.5 ppm conditions. **b** The Zeta potential of Cell-DG under different concentrations of fluoride ion solutions. **c** The comparison of Zeta potential between Cell-DG and Cell-NH in aqueous solution.



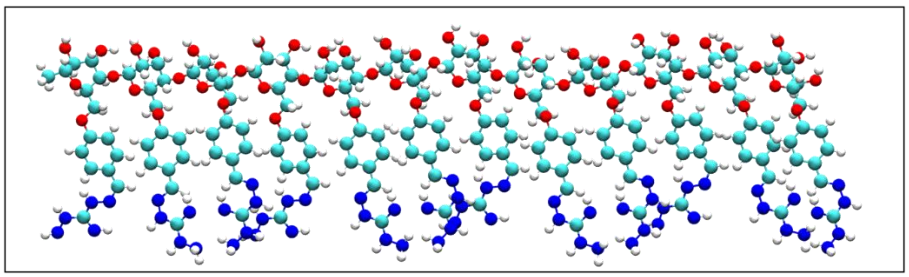
Supplementary Figure 18 Changes in the Zeta potential of Cell-DG$_2$ under different concentrations of NaCl.



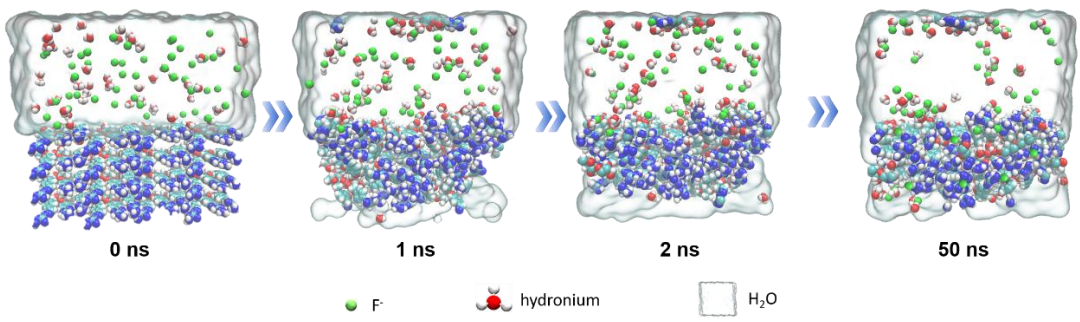
Supplementary Figure 19 FT-IR spectra of the guanidine-based polymer adsorbent Cell-DG_2 at different adsorption concentrations: **a** full spectrum, N-H bond, C=N bond and C-O-C bond. **b** changes in wavenumber with adsorption concentration.



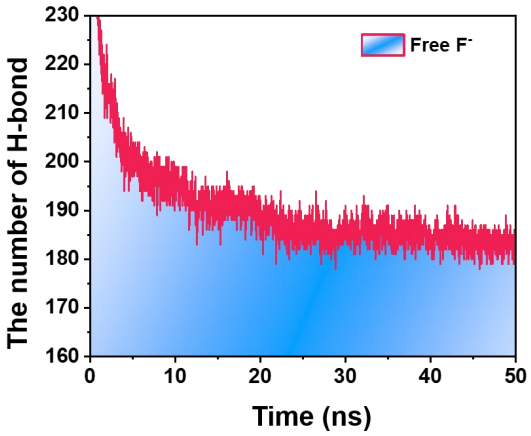
Supplementary Figure 20 a The full spectra of the guanidine-based cellulose polymer material Cell-DG_2 at 20, 40, 60, 80, 100, 120, 140 and 160 °C, and the FT-IR spectra of the N-H bond and C-O-C bond **b**.



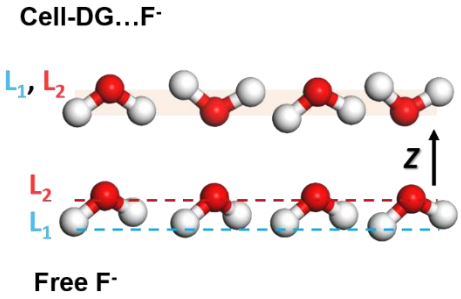
Supplementary Figure 21 Molecular model and optimized configuration of the guanidine-functionalized cellulose Cell-DG polymer chain.



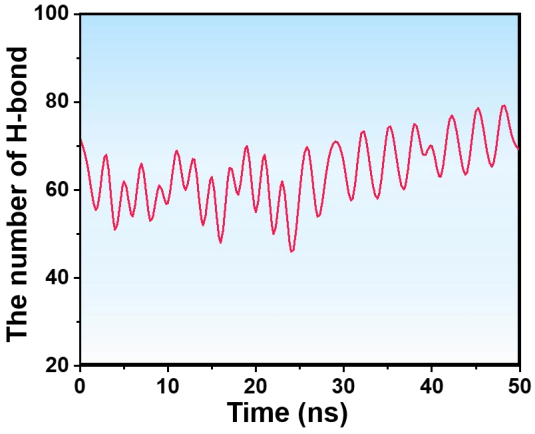
Supplementary Figure 22 Snapshots of the MD simulations of Cell-DG and fluoride solutions taken at 0 ns, 1 ns, 2 ns and 50 ns, respectively. Blue, cyan, red, and white balls represent N, C, O and H atoms, respectively.



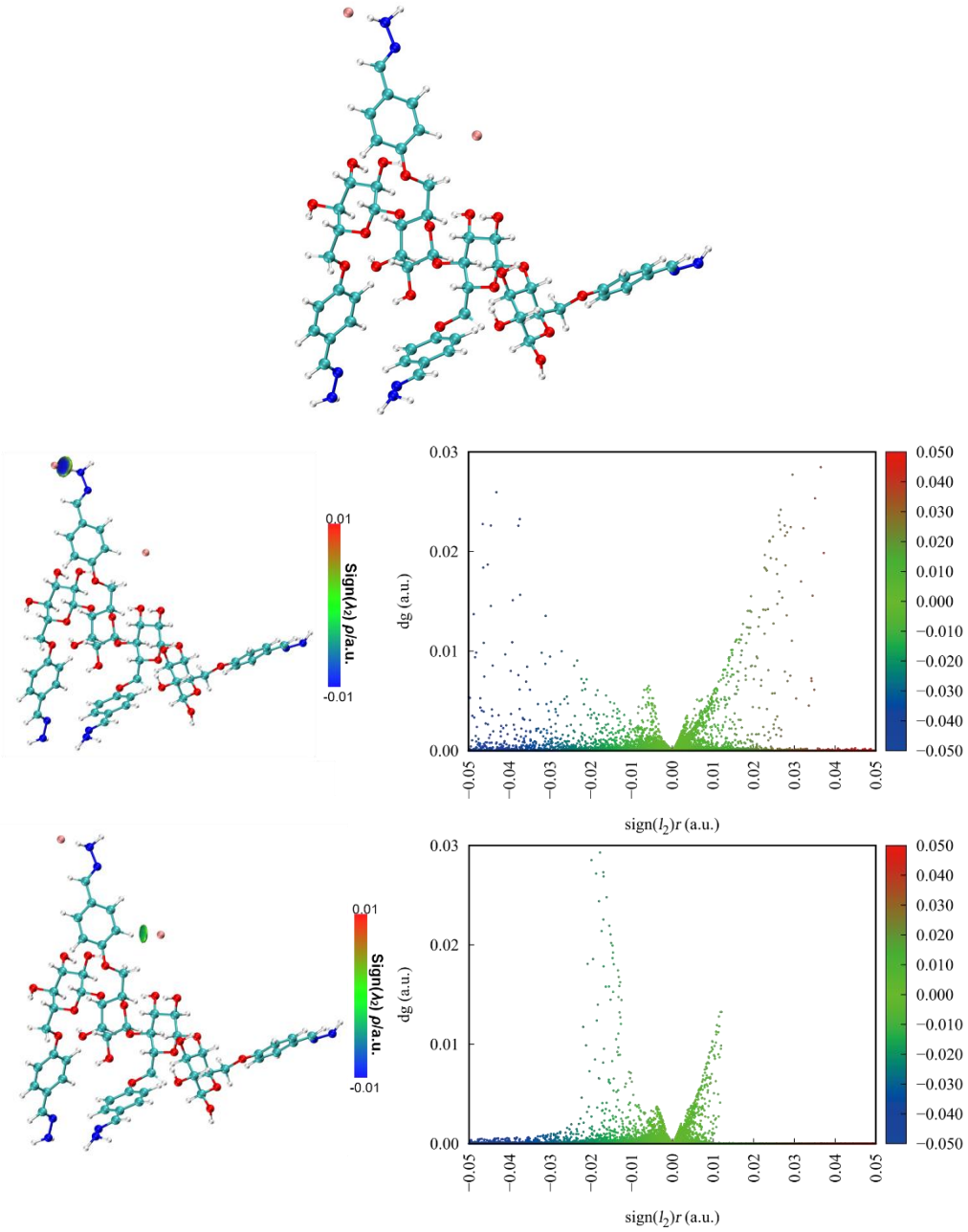
Supplementary Figure 23 The number of hydrogen bonds surrounding free fluoride ions.



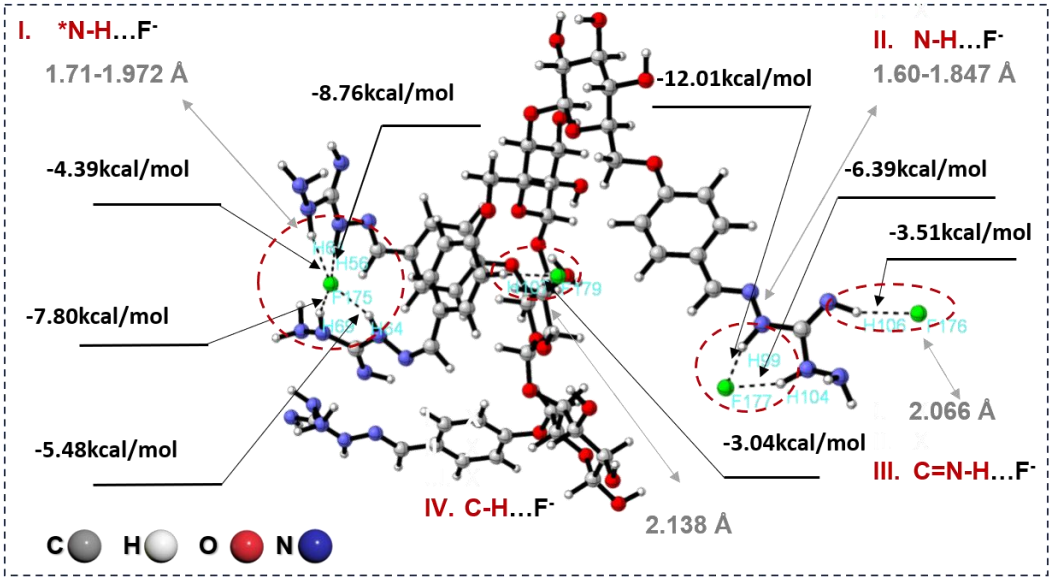
Supplementary Figure 24 Schematic diagram of H_2O configuration at the interface of free F^- and Cell-DG···F^-.



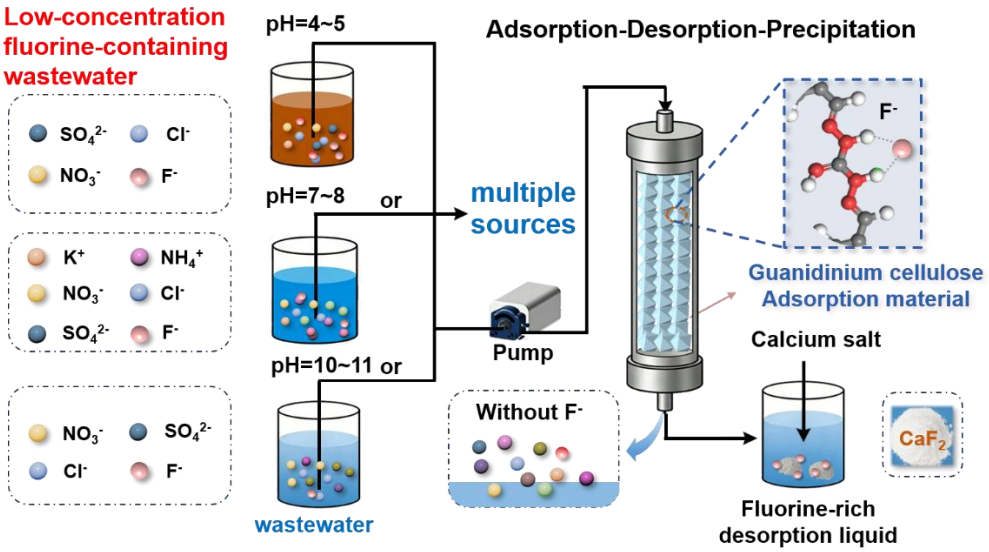
Supplementary Figure 25 Cell-DG captures the number of hydrogen bonds around F^-.



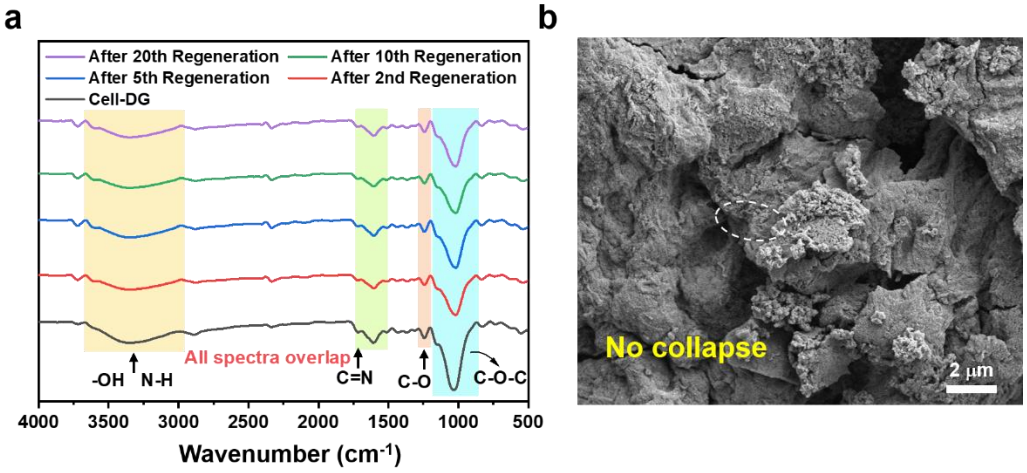
Supplementary Figure 26 Optimized structure of the Cell-NH•F^- complex at the B3LYP-D3/6-31G(d)/SMD(water) level of theory.



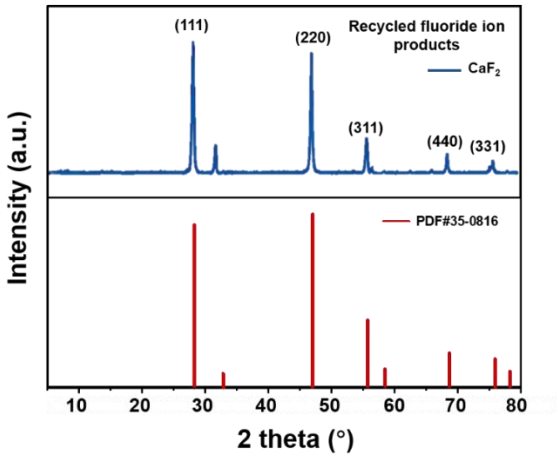
Supplementary Figure 27 Hydrogen bond energy Cell-DG···F^-.



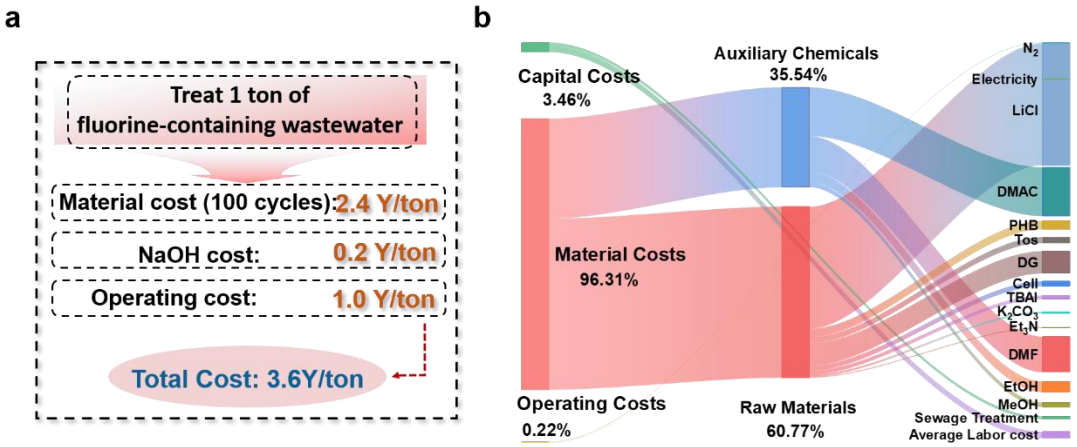
Supplementary Figure 28 Fixed-bed setup for continuous-flow treatment of simulated fluoride-bearing wastewaters using Cell-DG_2.



Supplementary Figure 29 a Comparative analysis of FT-IR spectra for Cell-DG_2 before and after adsorption and desorption. **b** SEM image of Cell-DG_2 after 20 desorption processes.



Supplementary Figure 30 XRD pattern of recovered CaF_2 from Cell-DG_2 packed column adsorption.



Supplementary Figure 31 a Process flow diagram for treating 1 ton of fluorine-containing wastewater. **b** The subdivided cost of polymer adsorbent preparation.

Supplementary Table S1 Water-quality characteristics of selected low-fluoride streams from photovoltaic, semiconductor and lithium-ion battery industries, with complementary model-water conditions.

Industrial sector	Stream and evidence basis	Fluoride (mg L^{-1})	pH	Coexisting constituents and matrix characteristics (mg L^{-1} unless otherwise specified)	Ref.
Photovoltaics	Induced-crystallization / solids-separation effluent; real wastewater, pilot scale	20-30	NR	NR	14
Photovoltaics	Chemical-precipitation effluent; full-scale plant	8-15	6-7	Hardness, 800-1400; conductivity, 3000-6000 μS cm^{-1}	15
Photovoltaics	Neutralization / precipitation filtrate; real solar-cell wastewater, pilot scale	12.46	6.85	Cl^-, 333; SO_4^{2-}, 85; HCO_3^-, 61; Na^+, 163; K^+, 75; Mg^{2+}, 30; Ca^{2+}, 215.8; Al, 15.3; TDS, 2472	16
Photovoltaics	Liquid phase after lime treatment of fluoride-bearing sludge; recovery-side stream	37	8.9[a]	Si, 76.8; Ca, 31.9; K, 4.8; Na, 3.4; Mg, 1.89	17
Semiconductors	Biologically treated production wastewater; real industrial effluent	4-7	6-8	Hardness, 9-11 mmol L^{-1}; COD, 20-30; SS, 18-24; individual ion concentrations, NR	18

Industrial sector	Stream and evidence basis	Fluoride (mg L^{-1})	pH	Coexisting constituents and matrix characteristics (mg L^{-1} unless otherwise specified)	Ref.
LIB recycling	Water-based direct physical recycling; real process water before targeted P/F removal	29.6-38.3[b]	7.1-7.4	Cl^-, 46.4-51.2; SO_4^{2-}, 39.1-45.2; Li, 127-157; Ca, 26.2-35; Na, 2.8-40.5; Mg, 6.0-7.3	19
Semiconductors (model water)	Synthetic NaF solutions for separate pH and competing-anion tests	6.0	2-8[c]	Cl^-, NO_3^-, SO_4^{2-} or HCO_3^- individually added at 0-400 in separate tests at pH ≈7	18
Semiconductors (model water)	Synthetic post-precipitation wastewater for electrocoagulation-flotation tests	42	3-11[c]	NaCl, 2000 (added supporting electrolyte)	20

PV, photovoltaic; LIB, lithium-ion battery; NR, not reported; TDS, total dissolved solids; COD, chemical oxygen demand; SS, suspended solids. Entries are selected examples, not an industry-wide distribution. Values belong to the stated stream; upstream concentrations and design limits are not transferred to treated water. Hardness is retained in the original units and is not a Ca^{2+} concentration. Elemental concentrations do not establish aqueous speciation.

[a] Treatment-adjusted pH. For the PV sludge-derived stream, values are from Table 3 of ref. 4; the separate liquid-phase data in Table 4 are not combined with this row.

[b] Free F^- only. Total fluorine is 123-468 mg L^{-1}, with PF_6^- and bis(fluorosulfonyl)imide also present; the ≤50 mg L^{-1} criterion applies to free fluoride in this case.

[c] Initial pH adjusted in synthetic-water experiments. These entries provide complementary experimental conditions, not measured industrial-water pH ranges; the pH and individual-anion tests in ref. 5 are separate experiments.

Supplementary Table S2 The C, H, N elemental content and mass fraction of grafted DG of Cell-DG $_{0,\ 0.5,\ 1,\ 2}$ with different guanidine salt feed ratios.

Sample	C (%)	H (%)	N (%)	DG mss fraction (%)	n_{DG} mmol /g
Cell-DG$_0$	41.639	5.781	0.120	0	0
Cell-DG$_{0.5}$	43.334	5.352	3.991	6.93	0.552
Cell-DG$_1$	41.934	5.223	4.083	7.10	0.566
Cell-DG$_2$	40.640	5.082	5.497	9.63	0.768

Supplementary Table S3 Specific surface area and pore volume of Cell-DG $_{0,\ 0.5,\ 1,\ 2}$.

Adsorbent	BET surface area (m^2/g)	Total pore volume (cm^3/g)	Average pore diameter (nm)
Cell-DG$_0$	8.09	0.045	3.68
Cell-DG$_{0.5}$	12.48	0.0691	4.07
Cell-DG$_1$	13.08	0.0754	3.61
Cell-DG$_2$	49.33	0.0905	2.63

Supplementary Table S4 Langmuir, Freundlich and Temkin isothermal adsorption model fitting parameters for F^- adsorption by Cell-DG $_{0,\ 0.5,\ 1,\ 2}$.

Adsorbent	Langmuir isotherm			Freundlich isotherm			Temkin isotherm	
	Q_m (mg/g)	K_L (L/mg)	R^2	K_F	$1/n_F$	R^2	b	R^2
Cell-DG$_0$	2.5	0.0175	0.281	0.744	0.2237	0.8169	0.4448	0.9076
Cell-DG$_{0.5}$	15.84	0.0194	0.511	6.569	0.1636	0.9348	1.8067	0.9639
Cell-DG$_1$	26.07	0.0078	0.915	11.685	0.1551	0.8742	2.8421	0.9413
Cell-DG$_2$	33.06	0.0707	0.988	16.173	0.1441	0.8970	3.1396	0.9397

Supplementary Table S5 Proposed primary and proposed secondary kinetic parameters for the adsorption of F^- by Cell-DG $_{0,\ 0.5,\ 1,\ 2}$. Fluoride ions at an initial concentration of 100 ppm and 13 ppm.

Adsorbent	Pseudo-first-order kinetics			Pseudo-second-order kinetics		
	Q_t (mg/g)	k_1 (L/min)	R^2	Q_t (mg/g)	k_2(g/(mg·min))	R^2
Cell-DG$_0$	2.25794	0.1231	0.98061	2.3971	0.06670	0.98266
Cell-DG$_{0.5}$	18.7365	1.1110	0.74591	19.361	0.08921	0.83841
Cell-DG$_1$	22.7747	0.4591	0.90806	23.327	0.03875	0.96706
Cell-DG$_2$	29.1795	0.5069	0.90183	29.918	0.03299	0.97012
Adsorbent	**Pseudo-first-order kinetics**			**Pseudo-second-order kinetics**		
	Q_t (mg/g)	k_1 (L/min)	R^2	Q_t (mg/g)	k_2(g/(mg·min))	R^2
Cell-DG$_2$	12.3197	0.5069	0.90184	12.6315	0.07815	0.96386

Supplementary Table S6 Fitted parameters of the Langmuir, Freundlich, and Dubinin-Radushkevich (D-R) isotherm models for fluoride (F^-) adsorption by Cell-DG$_2$.

Adsorbent	Langmuir isotherm			Freundlich isotherm			Dubinin-Radushkevich isotherm			
	Q_m (mg/g)	K_L (L/mg)	R^2	K_F	n_F	R^2	Q_m (mg/g)	K_{DR}	E (kJ/mol)	R^2
298 K	35.3711	0.9251	0.9721	17.2016	7.5870	0.8702	31.2922	0.8545	1.8950	0.92975
308 K	36.0898	0.8385	0.9775	17.1054	6.9130	0.8560	33.4187	1.2209	1.6390	0.86787
318 K	36.7487	0.7994	0.9733	17.5602	6.6970	0.8287	35.5042	1.6612	1.4510	0.88819

Supplementary Table S7 Basic thermodynamic parameters of F- adsorption by Cell-DG$_2$.

Cell-DG	ΔG (kJ/mol)	ΔH (kJ/mol)	ΔS (kJ/mol)
298 K	-3.865	30.7448	116.007

308 K	-4.904
318 K	-6.191

Supplementary Table S8 Comparison of adsorption properties (fluoride-adsorption equilibrium time, residual fluoride concentration and removal performance) of reported fluoride adsorption materials.

Type	Adsorbent	Equilibrium time (min)	Residual F^- concentration (ppm)	Removal (%)	Reference
Metal oxides/hydroxides and MOFs	Activated alumina (AA)	120	1.39	86.1	21
	MIL-96(Al)	90	4.77	68.20	22
	MOF-801	120	4.90	80.40	23
	NH_2-MIL-101(Al)	60	3.88	44.57	24
	Ferric hydroxide	120	4.23	57.75	25
	Magnesia-amended activated alumina	180	4.50	84.50	26
	Hydrous bismuth oxide (HBO_2)	180	4.90	51.00	27
Carbon-based and mineral materials	MWCNT-CH (cattle-horn HAp/MWCNT composite)	80	1.979	80.21	28
	Ce-Al-O/AC (activated-carbon-supported Ce-Al oxides)	120	1.084	89.16	29
	Hydroxyapatite (Xq-HAP)	180	3.20	68.00	30
	Mechanochemically	60	4.17	21.81	31

Type	Adsorbent	Equilibrium time (min)	Residual F^- concentration (ppm)	Removal (%)	Reference
	activated aluminosilicate clay				
	Alum-modified eggshell	68	4.90	29.96	32
	$Al(OH)_3$-coated activated carbon (AHAC)	70	4.58	54.21	33
	Surfactant-modified Na-LTA zeolite	60	3.54	64.60	34
	Xq-HAP	180	3.20	68.0	35
	CSLDO400 (calcined chitosan-supported LDH)	120	2.815	71.85	36
	SA@RM (sodium-alginate/red-mud adsorbent)	40	3.69	68.47	37
Biopolymer-based materials	Al_2O_3-nanolayer bacterial cellulose	60	3.95	20.96	38
	Sodium alginate-red mud (SA@RM)	40	3.69	68.47	39
	Modified coriander seeds	90	4.76	80.96	40
	Chitosan-coated calcium alginate (CCCA)	120	5.00	75.00	41

Type	Adsorbent	Equilibrium time (min)	Residual F^- concentration (ppm)	Removal (%)	Reference
	Fe_3O_4/graphene/alginate nanocomposite hydrogel	120	4.10	59.00	42
	Cell-DG	**6**	**0.096**	**99.68**	**This work**

Supplementary Table S9 IGM-derived geometric, energetic, and electronic descriptors for hydrogen bonds in the guanyl polymer system.

Hydrogen bond	Site	H…F (Å)	Bond angle (°)	Bond energy (kcal/mol)	ρ(r) (a.u.)	∇²ρ(r) (a.u.)	H(r) (a.u.)	ELF	LOL	ε
F177-H99	N17-H7…F3	1.594	160.8	-12.01	0.05725	0.1356	-0.01527	0.1977	0.3318	0.0155
F175-H56	N2-H1…F1	1.714	158.9	-8.76	0.04260	0.1242	-0.00628	0.1376	0.2855	0.0279
F175-H69	N8-H4…F1	1.747	166.5	-7.80	0.03829	0.1197	-0.00410	0.1187	0.2685	0.0173
F177-H104	N18-H8…F3	1.847	153.7	-6.39	0.03196	0.1072	-0.00117	0.0984	0.2484	0.0595
F175-H64	N7-H3…F1	1.801	161.6	-5.48	0.02791	0.0987	+0.00018	0.0831	0.2314	0.0559
F175-H61	N3-H2…F1	1.972	148.2	-4.39	0.02302	0.0886	+0.00175	0.0643	0.2077	0.0776
F176-H106	N19-H9…F2	2.066	156.2	-3.51	0.01907	0.0709	+0.00192	0.0576	0.1983	0.0179
F179-H107	C12-H10…F4	2.138	160.7	-3.04	0.01697	0.0654	+0.00236	0.0503	0.1872	0.0352

Supplementary Table S10 Water quality characteristics report on fluorine-containing process water and pretreatment wastewater in the photovoltaic, semiconductor, and lithium-ion battery industries.

NO.	Matrix characteristic	Fluoride (mg L^{-1})	pH	Coexisting constituents and matrix characteristics (mg L^{-1})
I	Acidic mixed-anion matrix	15.10	4.0 ± 0.1	Cl^-: 100, NO_3^-, 50; SO_4^{2-}: 100.
II	Near-neutral mixed-ion matrix	13.15	7.0 ± 0.1	Cl^-: 200, NO_3^-, 20; SO_4^{2-}: 50, NH_4^+: 10, K^+: 5.
III	Alkaline, elevated-salinity matrix	9.50	10.0 ± 0.1	Cl^-: 300, NO_3^-, 50; SO_4^{2-}: 150.

Supplementary Table S11 Prices of substances required to synthesize materials.

	Item	Martet price	Unit	Update date	Date source
1	cellulose	12.5	¥ /kg	31-Jan-25	GDC
2	Lithium chloride	60	¥ /kg	31- Jan-25	100PPI
3	Tos	12	¥ /kg	31- Jan-25	GDC
4	Et_3N	5	¥ /kg	31-Jan-25	GDC
5	PHB	12	¥ /kg	31-Jan-26	GDC
6	K_2CO_3	7.4	¥ /kg	31-Jan-26	GDC
7	TBAI	25	¥ /kg	31-Jan-26	GDC
8	DG	50	¥ /kg	31-Jan-26	1688
9	DMF	7	¥ /kg	31-Jan-26	GDC
10	DMAC	4.8	¥ /kg	31-Jan-26	GDC
11	EtOH	5.4	¥ /kg	31-Jan-26	100PPI
12	MeOH	2.3	¥ /kg	31- Jan-26	100PPI
13	Electricity	0.69	¥ /Kw/h	31- Jan-26	Sci99
14	N_2	10.85	¥ /kg	31-Jan-26	Sci99
15	Average labor cost	80000	¥ /a	31-Jan-26	JOBUI
16	Sewage treatment	3	¥ /t	31-Jan-26	BDB

① Chemical raw materials are industrial grade.

② $ = 6.99 ¥ (Update time: 2026/1/31).

③ Data Sources: GDC (https://china.guidechem.com/)

1688 (https://detail.1688.com/)

100PPI (http://www.100ppi.com/ppi)

Supplementary References

1. Becke, A. D. Density-functional thermochemistry. III. The role of exact exchange. *J. Chem. Phys.* **98**, 5648-5652 (1993).

2. Lee, C., Yang, W. & Parr, R. G. Development of the Colle-Salvetti correlation-energy formula into a functional of the electron density. *Phys. Rev. B* **37**, 785-789 (1988).

3. Grimme, S., Antony, J., Ehrlich, S. & Krieg, H. A consistent and accurate ab initio parametrization of density functional dispersion correction (DFT-D) for the 94 elements H-Pu. *J. Chem. Phys.* **132**, 154104 (2010).

4. Francl, M. M., Petro, W. J., Hehre, W. J., Binkley, J. S., Gordon, M. S., DeFrees, D. J. & Pople, J. A. Self-consistent molecular orbital methods. XXIII. A polarization-type basis set for second-row elements. *J. Chem. Phys.* **77**, 3654-3665 (1982).

5. Neese, F. Software update: the ORCA program system-version 6.0. *WIREs Comput. Mol. Sci.* **15**, e70019 (2025).

6. Brandenburg, J. G., Bannwarth, C., Hansen, A. & Grimme, S. B97-3c: a revised low-cost variant of the B97-D density functional method. *J. Chem. Phys.* **148**, 064104 (2018).

7. Barone, V. & Cossi, M. Quantum calculation of molecular energies and energy gradients in solution by a conductor solvent model. *J. Phys. Chem. A* **102**, 1995-2001 (1998).

8. Adamo, C. & Barone, V. Toward reliable density functional methods without adjustable parameters: the PBE0 model. *J. Chem. Phys.* **110**, 6158-6170 (1999).

9. Caldeweyher, E., Ehlert, S., Hansen, A., Neugebauer, H., Spicher, S., Bannwarth, C. & Grimme, S. A generally applicable atomic-charge dependent London dispersion correction. *J. Chem. Phys.* **150**, 154122 (2019).

10. Weigend, F. & Ahlrichs, R. Balanced basis sets of split valence, triple zeta valence and quadruple zeta valence quality for H to Rn: design and assessment of accuracy. *Phys. Chem. Chem. Phys.* **7**, 3297-3305 (2005).

11. Rappoport, D. & Furche, F. Property-optimized Gaussian basis sets for molecular response calculations. *J. Chem. Phys.* **133**, 134105 (2010).

12. Lu, T. & Chen, Q. Independent gradient model based on Hirshfeld partition: a new method for visual study of interactions in chemical systems. *J. Comput. Chem.* **43**, 539-555 (2022).

13. Lu, T. & Chen, F. Multiwfn: a multifunctional wavefunction analyzer. *J. Comput. Chem.* **33**, 580-592 (2012).

14. Hu, R., Tian, Z., Fan, Z., Huang, T. & Wen, G. Pilot test on acidic fluoride-containing wastewater treatment in the photovoltaic industry through induced crystallization with a focus on calcium fluoride recovery. *Sep. Purif. Technol.* **341**, 126879 (2024).

15. Wang, Y. & Liu, Q. Case study-fluoride wastewater from photovoltaic industry recycled. *J. Chem. Pharm. Res.* **6**, 468-472 (2014).

16. El Diwani, G., Amin, S. K., Attia, N. K. & Hawash, S. I. Fluoride pollutants removal from industrial wastewater. *Bull. Natl. Res. Cent.* **46**, 143 (2022).

17. Zueva, S. et al. An effective new treatment of fluoride-containing sludge resulting from the manufacture of photovoltaic cells. *Processes* **9**, 1745 (2021).

18. Lu, Y. et al. Advanced treatment of fluoride wastewater by chemical precipitation and nanomaterial adsorption. *Ind. Water Treat.* **42**, 75-79 (2022).

19. Wagner-Wenz, R. et al. Removal and recovery of phosphorus and fluorine in process water from water based direct physical lithium-ion battery recycling. *Water Res.* **268**, 122476 (2025).

20. Aoudj, S., Khelifa, A., Drouiche, N. & Hecini, M. Development of an integrated electro-coagulation–flotation for semiconductor wastewater treatment. *Desalin. Water Treat.* **55**, 1422-1432 (2015).

21. Dhawane, S. H., Khan, A. A., Singh, K., Tripathi, A., Hasda, R. & Halder, G. Insight into optimization, isotherm, kinetics, and thermodynamics of fluoride adsorption onto activated alumina. *Environ. Prog. Sustain. Energy* **37**, 766-776 (2018).

22. Wang, X. et al. Synthesis and study of an efficient metal-organic framework adsorbent (MIL-96(Al)) for fluoride removal from water. *J. Nanomater.* **2019**, 3128179 (2019).

23. Tan, T. L., Krusnamurthy, P. A., Nakajima, H. & Rashid, S. A. Adsorptive, kinetics

and regeneration studies of fluoride removal from water using zirconium-based metal organic frameworks. *RSC Adv.* **10**, 18740-18752 (2020).

24. Luo, Y. et al. Mechanism of enhanced fluoride adsorption using amino-functionalized aluminum-based metal-organic frameworks. *Water* **16**, 2889 (2024).

25. Sujana, M. G. & Anand, S. Ferric hydroxide: preparation, characterisation and fluoride removal studies from water. *Desalin. Water Treat.* **52**, 645-6463 (2014).

26. Maliyekkal, S. M., Shukla, S., Philip, L. & Nambi, I. M. Enhanced fluoride removal from drinking water by magnesia-amended activated alumina granules. *Chem. Eng. J.* **140**, 183-192 (2008).

27. Srivastav, A. L., Singh, P. K. & Sharma, Y. C. Synthesis of a novel adsorbent, hydrous bismuth oxide (HBO_2), for the removal of fluoride from aqueous solutions. *Desalin. Water Treat.* **55**, 604-614 (2015).

28. William, O., Meshesha, B. T., Mussa, M., Gebreeyessus, G. D. & Zewge, F. Highly efficient $Al(OH)_3$/HAp composite adsorbent for the removal of fluoride from drinking water: batch and column studies. *Appl. Water Sci.* **15**, 188 (2025).

29. Akafu, T., Chimdi, A. & Gomoro, K. Removal of fluoride from drinking water by sorption using diatomite modified with aluminum hydroxide. *J. Anal. Methods Chem.* **2019**, 4831926 (2019).

30. Zou, Y. et al. Preparation of hydroxyapatite and its elimination of excess fluoride from aqueous solution. *RSC Adv.* **14**, 26103-26114 (2024).

31. Obijole, O. A., Gitari, M. W., Ndungu, P. G. & Samie, A. Mechanochemically activated aluminosilicate clay soils and their application for defluoridation and pathogen removal from groundwater. *Int. J. Environ. Res. Public Health* **16**, 654 (2019).

32. Hosseini, S. S., Pasalari, H., Yousefi, N. & Mahvi, A. H. Eggshell modified with alum as low-cost sorbent for the removal of fluoride from aquatic environments: isotherm and kinetic studies. *Desalin. Water Treat.* **146**, 326-332 (2019).

33. Amalraj, A. & Pius, A. Removal of fluoride from drinking water using aluminum hydroxide coated activated carbon prepared from bark of Morinda tinctoria. *Appl. Water Sci.* **7**, 2653-2665 (2017).

34. Ebsa, D. G. Defluoridation of drinking water by modified natural zeolite with

cationic surfactant, in the case of Ziway town, Ethiopia. *Clean. Eng. Technol.* **12**, 100596 (2023).

35. Wang, J., Zhang, H., Wang, N., Mo, H., Yang, Z., Dong, Y., Liu, Q., Huang, X. & Han, B. Synthesis of polymer sodium alginate-red mud adsorbent and its application in the removal of low-concentration fluoride. *Polymers* **17**, 826 (2025).

36. Li, X., Guo, Y., Xie, Y. & Sun, Y. Treatment of fluorinated wastewater with chitosan modified activated sludge lysis ash. *RSC Adv.* **12**, 34006-34019 (2022).

37. Zou, Y., Wang, Y., Wang, J., Wang, S., Chen, L., Xi, Y., Xie, R., Yang, J. & Xiao, X. Preparation of hydroxyapatite and its elimination of excess fluoride from aqueous solution. *RSC Adv.* **14**, 26103-26114 (2024).

38. Dolganov, A. V., Revin, V. D., Kostryukov, S. G., Revin, V. V. & Yang, G. Kinetic and thermodynamic characteristics of fluoride ions adsorption from solution onto the aluminum oxide nanolayer of a bacterial cellulose-based composite material. *Polymers* **13**, 3421 (2021).

39. Wang, J. et al. Synthesis of polymer sodium alginate-red mud adsorbent and its application in the removal of low-concentration fluoride. *Polymers* **17,** 826 (2025).

40. Moradi, F., Shirmohammadi, S., Zarei, A. & Rezaei, M. Application of modified coriander seeds as biomaterial for removal of fluoride from aqueous media. *Desalin. Water Treat.* **180**, 271-283 (2020).

41. Vijaya, Y., Popuri, S. R., Reddy, G. S. & Krishnaiah, A. Development and characterization of chitosan coated biopolymer sorbent for the removal of fluoride ion from aqueous solutions. *Desalin. Water Treat.* **25**, 159-169 (2011).

42. Kumari, S., Singh, N., Sharma, R., Yadav, M. & Khan, S. Kinetics and isotherms of adsorption of fluoride onto Fe_3O_4/graphene/alginate nanocomposite hydrogel. *Environ. Nanotechnol. Monit. Manag.* **16**, 100590 (2021).